2015

THE N-P SCATTERING CROSS SECTION FROM 90 KEV TO 1.8 MEV

Hongwei Yang
University of Kentucky, yhw1630@gmail.com

STUDENT AGREEMENT:

I represent that my thesis or dissertation and abstract are my original work. Proper attribution has been given to all outside sources. I understand that I am solely responsible for obtaining any needed copyright permissions. I have obtained needed written permission statement(s) from the owner(s) of each third-party copyrighted matter to be included in my work, allowing electronic distribution (if such use is not permitted by the fair use doctrine) which will be submitted to UKnowledge as Additional File.

I hereby grant to The University of Kentucky and its agents the irrevocable, non-exclusive, and royalty-free license to archive and make accessible my work in whole or in part in all forms of media, now or hereafter known. I agree that the document mentioned above may be made available immediately for worldwide access unless an embargo applies.

I retain all other ownership rights to the copyright of my work. I also retain the right to use in future works (such as articles or books) all or part of my work. I understand that I am free to register the copyright to my work.

REVIEW, APPROVAL AND ACCEPTANCE

The document mentioned above has been reviewed and accepted by the student's advisor, on behalf of the advisory committee, and by the Director of Graduate Studies (DGS), on behalf of the program; we verify that this is the final, approved version of the student's thesis including all changes required by the advisory committee. The undersigned agree to abide by the statements above.

Hongwei Yang, Student

Dr. Michael A. Kovash, Major Professor

Dr. Tim Gorringe, Director of Graduate Studies

THE N-P SCATTERING CROSS SECTION FROM 90 KEV TO 1.8 MEV

DISSERTATION

A dissertation submitted in partial fulfillment of the
requirements for the degree of Doctor of Philosophy in the
College of Arts and Sciences
at the University of Kentucky

By
Hongwei Yang
Lexington, Kentucky

Director: Dr. Michael A. Kovash, Professor of Physics and Astronomy
Lexington, Kentucky 2015

ABSTRACT OF DISSERTATION

THE N-P SCATTERING CROSS SECTION FROM 90 KEV TO 1.8 MEV

There have been very few measurements of the total cross section for n-p scattering below 500 keV. In order to differentiate among NN potential models, improved cross section data between 20 and 600 keV are required. We measured the n-p and n-C total cross sections in this energy region by transmission; a collimated neutron beam was passed through CH_2 and C samples and transmitted neutrons were detected by a BC-501A deuterated liquid scintillator. Cross sections were obtained by taking the ratios of normalized neutron yields with the samples in the beam and with no sample in the beam. Both better precision and larger range between 90 keV and 1.8 MeV results are presented. The parameters resulting from fitting effective range theory to the data for n-p scattering are in good agreement with parameters determined from previous fits.

KEYWORDS: Nucleon Nucleon Interaction, Effective Range theory, Neutron Beam, Cross Section, Scattering Length

Author's signature: Hongwei Yang

Date: July 11, 2015

THE N-P SCATTERING CROSS SECTION FROM 90 KEV TO 1.8 MEV

By
Hongwei Yang

Director of Dissertation: Michael A. Kovash

Director of Graduate Studies: Tim Gorringe

Date: July 11, 2015

Dedicated to the prosperity of human being.

ACKNOWLEDGMENTS

I want to thank University of Kentucky for giving me the chance to carry out this project.

I also want to thank Dr. Kovash for being my advisor for all these 6 years. For all the major difficulties I have encounted these years, it is Dr. Kovash's strong support helped me moving forward every time. It is also Dr. Kovash, from his continuous encouragement, month my month, year by year, helped me build up my confident and freed up my mind to get things done creatively. No hesitate to say, if I am the one who made this work valuable, Dr. Kovash is the one who made me valuable.

Zach Miller, my working partner, but more of a friend in need, is always the first one I'm asking for help. I will never forget the days we spend together on preparing numerous experiments and talking about 'sparkling' ideas.

And Greg Porter, Gene Barber and Erin Peters from shops and accelerator labs, their generous helps and kindly concerns also made my uncertain experiments under more control.

I would like to say a sepcial thanks to all my committee members: Dr. Renee Fatemi, Dr. Keh-Fei Liu, Dr. Steven Yates and Dr. Yuming Zhang. Their valuable suggestions from both theoretical and experimental perspects made this project even more meaningful.

There are more people I should mention but limited by the words in this page. I want say thanks to them here too.

Finally, as always, my family, dispite all the challenges we face over the years, they made me stay.

TABLE OF CONTENTS

LIST OF FIGURES

LIST OF TABLES

Chapter 1 Introduction

1.1 The Nucleon-Nucleon Interaction

Understanding the nucleon-nucleon (NN) interaction is one of the most fundamental and longstanding goal in nuclear physics; it has been the focus of attention ever since the field was born in 1932 with the discovery of the neutron by Chadwick [1]. It has been investigated by a large number of physicists all over the world for the past 80 years, which makes it the best known piece of strong interactions. Massive amounts of experimental data have been accumulated.

Yukawa's explanation using the boson (meson) exchange concept [2] was the first attempt to explain the nature of the nuclear force. Although this idea is not considered as fundamental anymore when comparing with QCD, it is still the best working model for a quantitative NN potential.

1.1.1 Isospin

Isospin (isotopic spin, isobaric spin) is a quantum number related to the strong interaction. Particles that are affected equally by the strong force but have different charges (e.g. protons and neutrons) can be treated as being different states of the same particle with isospin values related to the number of charge states.

Although it does not have the units of angular momentum and is not a type of spin, it is formally treated as a quantum mechanical angular momentum. For example, both the proton and the neutron have isospin $\frac{1}{2}$, with the proton assigned $+\frac{1}{2}$ to the z component T_z, and the neutron $T_z = -\frac{1}{2}$. Then it is clear that a proton-neutron pair can be in a state of total isospin 1 or 0. In the isospin $T = 1$ state, NN interactions can be characterized by T_z, proton-proton (p-p), neutron-proton (n-p), and neutron-neutron (n-n) interactions have T_z = +1, T_z = 0, and T_z = -1, respectively.

Observation of the light baryons (those made of up, down and strange quarks) lead us to believe that some of these particles are so similar in terms of their strong interactions that they can be treated as different states of the same particle. In the modern understanding of quantum chromodynamics, this is because up and down quarks are very similar in mass, and have the same strong interactions.

In quantum mechanics, when a Hamiltonian has a symmetry, that symmetry manifests itself through a set of states that have the same energy; that is, the states are degenerate. In particle physics, the near mass-degeneracy of the neutron and proton points to an approximate symmetry of the Hamiltonian describing the strong interactions. The neutron does have a slightly higher mass due to isospin breaking; this is due to the difference in the masses of the up and down quarks and the effects of the electromagnetic interaction.

1.1.2 Charge dependence

Charge independence is defined as invariance under any rotation in isospin space. A violation of this symmetry is called charge independence breaking (CIB). A special case of charge dependence is charge symmetry. Charge symmetry means invariance under a rotation by 180^0 about the y-axis in isospin space if the positive z-direction is associated with the positive charge. The violation of this symmetry is called charge symmetry breaking (CSB).

In strong NN interactions, CSB refers to a difference between p-p and n-n interactions only. CIB means that, in the isospin $T = 1$ state, after electromagnetic effects been removed, the p-p, n-p, and n-n interactions are slightly different. The charge dependence of the NN interaction is subtle, but in the ${}^1S_0$ state, the scattering length becomes sensitive to it, so charge-dependent effects can be observed by measuring the scattering length in this state.

The current understanding is that, on a fundamental level, the charge dependence of nuclear forces is due to a difference between the up and down quark masses and electromagnetic interactions among the quarks. A consequence of this is mass differences between hadrons of the same isospin multiplet and meson mixing. Therefore, if CIB is calculated based upon hadronic models, the mass differences between hadrons of the same isospin multiplet, meson mixing, and irreducible meson-photon exchanges are considered as major causes [3–5].

Ignoring CSB, the CIB differences in the effective range parameters are given by:

$$\Delta a_{CIB} \equiv \frac{1}{2}(a_{pp}^N + a_{nn}^N) - a_{np} = 5.640.60 \text{ fm}, \tag{1.1}$$

$$\Delta r_{CIB} \equiv \frac{1}{2}(r_{pp}^N + r_{nn}^N) - r_{np} = 0.03 \pm 0.13 \text{ fm}. \tag{1.2}$$

where a is the scattering length, and r is the effective range, N means the values are pure nucler value. Derivation of a and r will be shown later in section 1.2.

The major cause of CIB in the NN interaction is pion mass splitting (mass difference between π^0 and $\pi^{\pm}$). Based upon the Bonn Full Model for the NN interactions [6], the CIB due to pion mass splitting has been calculated carefully and systematically [7]. A varity of classes of diagrams and their contributions are calculated in [1]. One pion exchange (OPE) contributes the most, in which the CIB effect is created by replacing the diagram Figure 1.1 (a) by the two diagrams Figure 1.1 (b).

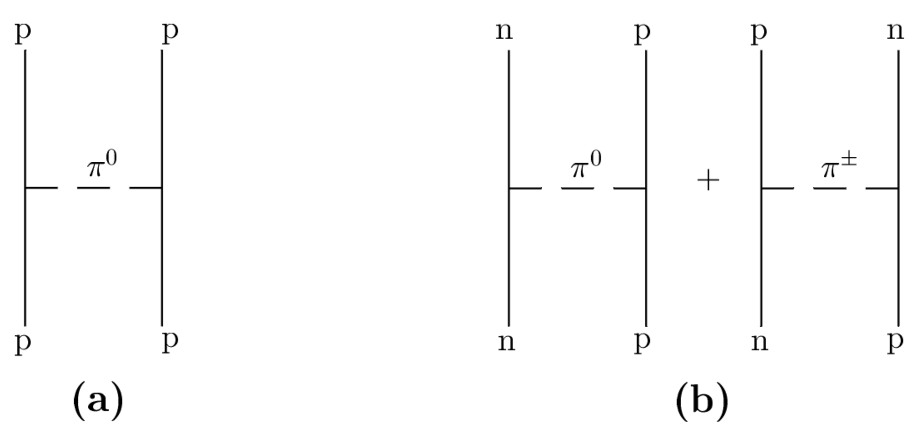

Figure 1.1: One pion exchange (OPE) contributions to (a) p-p and (b) n-p scattering.

To demonstrate the effect caused by this replacement, in nonrelativistic approximation and disregarding isospin factors, OPE is given by [7]

$$V_{1\pi}(g_\pi, m_\pi) = -\frac{g_\pi^2}{4M^2}\frac{(\boldsymbol{\sigma}_1 \cdot \boldsymbol{k})(\boldsymbol{\sigma}_2 \cdot \boldsymbol{k})}{m_\pi^2 + \boldsymbol{k}^2} F_{\pi NN}^2(\Lambda_{\pi NN}, |\boldsymbol{k}|) \tag{1.3}$$

where M is the average nucleon mass, m_π is the pion mass, and $\boldsymbol{k}$ is the momentum transfer. The above expression includes a πNN vertex form-factor, $F_{\pi NN}$, which depends on the cutoff mass $\Lambda_{\pi NN}$ and the magnitude of the momentum transfer $|\boldsymbol{k}|$. For $S = 0$ and $T = 1$, where S and T denote the total spin and isospin of the two-nucleon system, respectively, we have

$$ {}^{01}V_{1\pi}(g_\pi, m_\pi) = \frac{g_\pi^2}{m_\pi^2 + \boldsymbol{k}^2} \frac{\boldsymbol{k}^2}{4M^2} F^2_{\pi NN}(\Lambda_{\pi NN}, |\boldsymbol{k}|) \tag{1.4} $$

where the superscripts 01 refer to ST. In the ${}^1S_0$ state, this potential expression is repulsive. The charge-dependent OPE is then,

$$ {}^{01}V_{1\pi}^{pp} = {}^{01}V_{1\pi}(g_{\pi^0}, m_{\pi^0}) \tag{1.5} $$

for p-p scattering, and

$$ {}^{01}V_{1\pi}^{np} = 2\,{}^{01}V_{1\pi}(g_{\pi^\pm}, m_{\pi^\pm}) - {}^{01}V_{1\pi}(g_{\pi^0}, m_{\pi^0}) \tag{1.6} $$

for n-p scattering. If we assume g_π (i.e., $g_{\pi^0} = g_{\pi^\pm}$) are charge-independent, then all CIB comes from the charge splitting of the pion mass, which is [8]

$$ m_{\pi^0} = 134.977 \text{ MeV} \tag{1.7} $$

$$ m_{\pi^\pm} = 139.570 \text{ MeV} \tag{1.8} $$

Since the pion mass appears in the denominator of OPE, the smaller π^0 mass exchanged in p-p scattering generates a larger (repulsive) potential in the ${}^1S_0$ state as compared to n-p where also the heavier $\pi^\pm$ mass is involved. Moreover, the π^0 exchange in n-p scattering carries a negative sign, which further weakens the n-p OPE potential. The bottom line is that the p-p potential is more repulsive than the n-p potential. The quantitative effect on Δa_{CIB} is such that it explains about 60% of the empirical value. Due to the small mass of the pion, OPE is a sizable contribution in all partial waves including higher partial waves; and due to the pions relatively large mass splitting (3.4%), OPE creates relatively large charge-dependent effects in all partial waves.

As a result, all contributions from meson exchanges including one-pion-exchange, 2π exchanges, $\pi\rho$ exchanges, and further 3π and 4π contributions $(\pi\sigma + \pi\omega)$ explain about 80% of Δa_{CIB} for singlet scattering length.

Moreover, OPE dominates the CIB effect in all partial waves, even though there are substantial contributions besides OPE in some states, notably $^1S_0$ and $^3P_1$.

Although the effect of ρ-mass splitting on the $^1S_0$ effective range parameters was also investigated [7], the evidence for ρ-mass splitting is very uncertain [8]. As a result, the effects from one-rho-exchange, and non-iterative $\pi\rho$ diagrams with NN intermediate states are small. And, in addition, the net result is even smaller because there are substantial cancellations between the two classes of diagrams that contribute. Hence, the ρ-mass splitting will not a great source of CIB event if it will be better known one day.

Once it was believed that the contribution of irreducible pion-photon $(\pi\gamma)$ exchange would take care of the remaining 20% of Δa_{CIB} [9–11]. In contrast, however, a derived $\pi\gamma$ potential based upon chiral perturbation theory [12] decreases Δa_{CIB} by about 0.5 fm, making the discrepancy even larger.

The result is, about 25% of the charge-dependence of the singlet scattering length is still not explained at this time.

In summary, the problem is that [1]

> quantitative models for the nuclear force have only a poor theoretical background, while theory based models yield only poor results. This discrepancy between theory and practice has become larger rather than smaller.

And the 'theory based models' are not strictly derived from QCD; they are modeled after QCD, often with handwoven arguments. Therefore, future research on the nuclear force must overcome the above discrepancies.

1.2 Effective Range Theory

If the incident energy is small enough, the S-wave ($l = 0$) only becomes effective, then effective range theory can be used to calculate cross sections for two body system.

Consider a neutron of energy E_1 and wave number k_1. If E_1 is in the laboratory system,

$$E_1 = \frac{2\hbar^2 k_1^2}{M} \tag{1.9}$$

Let u_1 be the radial wave function multiplied by r, for an S state; then u_1 statisfies the Schr$\ddot{o}$dinger equation

$$\frac{d^2u_1}{dr^2} + k_1^2 u_1 - V(r)u_1 = 0 \tag{1.10}$$

where V is the potential energy, multiplied by $M/\hbar^2$. For another energy, we have

$$\frac{d^2u_2}{dr^2} + k_2^2 u_2 - V(r)u_2 = 0 \tag{1.11}$$

Multiply (1.10) by u_2 and (1.11) by u_1, subtract and integrate; then,

$$u_2 u_1' - u_1 u_2'|_0^R = (k_2^2 - k_1^2) \int_0^R u_1 u_2 dr, \tag{1.12}$$

where the upper limit R is arbitrary.

If R is infinity, the orthogonality relation results. If R is chosen equal to the range of the nuclear forces, one obtains the relation of Bethe and Peierls [13] between scattering phase shift and k. We shall not use (1.12) directly, but first introduce a comparison function ψ which represents the asymptotic behavior of u for large distances, viz.

$$\psi_1 = A_1 sin(k_1 r + \delta_1) \tag{1.13}$$

where δ_1 is the phase shift for energy E_1. It is most convenient to choose the normalizing factor A_1 so as to make $\psi = 1$ at the origin, thus:

$$\phi_1 = \frac{sin(k_1 r + \delta_1)}{sin\delta_1} \tag{1.14}$$

This will at the same time determine the normalization of u, as u is supposed to approach ψ asymptotically for large r including normalization.

For the ψ's, a relation analogous to (1.12) will hold, viz.:

$$\psi_2\psi_1' - \psi_1\psi_2'|_0^R = (k_2^2 - k_1^2)\int_0^R \psi_1\psi_2 dr \tag{1.15}$$

Now subtract (1.12) from (1.15). Then, if the upper limit R is chosen large compared with the range of the nuclear forces, each function u_i will be equal to its asymptotic form ψ_i and there will, therefore, be no contribution to the integrated term (left-hand side) from the upper limit R. For the same reason, the integral on the right-hand side can now be extended to infinity. At the lower limit, $u_1 = u_2 = 0$ so that this term does not contribute. This leaves

$$(\psi_1\psi_2' - \psi_2\psi_1')_{r=0} = (k_2^2 - k_1^2)\int_0^\infty (\psi_1\psi_2 - u_1u_2)dr \tag{1.16}$$

Now we have normalized ψ to unity at $r = 0$ (1.14) , and the derivative of ψ can easily be obtained from (1.14), so that we find

$$k_2 cot\delta_2 - k_1 cot\delta_1 = (k_2^2 - k_1^2)\int_0^\infty (\psi_1\psi_2 - u_1u_2)dr \tag{1.17}$$

This equation is exact and is the fundamental equation of our theory.

We can now apply (1.17) to the special case $k_1 = 0$. Then

$$k_1 cot\delta_1 = -\alpha \equiv -\frac{1}{a} \tag{1.18}$$

where a is the scattering length of Fermi and Marshall [14], for zero-energy neutrons, which can be determined with great accuracy. For the triplet state, a is positive, for the singlet state, negative. We shall use subscripts zero for the wave functions referring to zero energy, and we may drop the subscripts for state 2. Then (1.17) becomes

$$k cot\delta = -\alpha + \frac{1}{2}k^2\rho(0, E) \tag{1.19}$$

with

$$\frac{1}{2}\rho(0, E) = \int_0^\infty (\psi_0\psi - u_0u)dr \tag{1.20}$$

Clearly, ρ has the dimension of a length. It can also be defined for two arbitrary energies,

$$\frac{1}{2}\rho(E_1, E_2) = \int_0^\infty (\psi_1\psi_2 - u_1u_2)dr \tag{1.21}$$

The important point is now that ψ and u differ only inside the range of the nuclear forces. Therefore the integrands in (1.20) and (1.21) will be different from zero only inside the force-range. However, in this region the wave functions u and ψ depend only very slightly on energy, because kr is small and the potential energy is much larger than k^2. Therefore, it will be a good appoximation (indeed a very good one, as we shall show in the next section) to replace u by u_0 and ψ by ψ_0 and to write

$$\frac{1}{2}\rho(0,E) \approx \frac{1}{2}\rho(0,0) \equiv \frac{1}{2}r_0 = \int_0^\infty (\psi_0^2 - u_0^2)dr \tag{1.22}$$

This quantity is now a constant, independent of energy, and we call it the effective range [15]. It is identical with the effective range used and defined by Blatt and Jackson [16]. (For the shape of the functions ψ_0 and u_0 see their Fig. 3.) Schwinger [17] defined r_0 by

$$\frac{1}{2}r_0 = \int_0^\infty (\psi_g^2 - u_g^2)dr \tag{1.23}$$

where u, and ψ_g refer to the ground state of the deuteron, and in particular ψ_g is the asymptotic solution

$$\psi_g = e^{\gamma r} \tag{1.24}$$

where γ is related to the deuteron binding energy, ϵ, by $\epsilon = (\hbar^2/M)\gamma^2$ [17]. Since $\rho(E_1, E_2)$ is insensitive to the energies E_1, and E_2, it makes little difference if both of them are replaced by $-\epsilon$ where ϵ is the binding energy of the deuteron. Blatt and Jackson have shown that (1.22) will give a somewhat closer approximation to the scattering than (1.23).

Using (1.22), then, the fundamental relation (1.19) reduces to

$$kcot\delta = -\alpha + \frac{1}{2}k^2 r_0 \tag{1.25}$$

The exact neutron-proton s-wave elastic cross section is [18]

$$\sigma = \frac{3}{4}\sigma_t + \frac{1}{4}\sigma_s \tag{1.26}$$

$$\sigma_d = \frac{4\pi}{\left(\left(\frac{1}{a_d} - \frac{1}{2}\rho_d(0,T)p^2\right)^2 + p^2\right)} \tag{1.27}$$

where the subscript d is t for the triplet or s for the singlet, a_d is the scattering length, and $\rho_d(0,T)$ is the energy-dependent effective range. T and p are the center-of-mass (c.m.) kinetic energy and momentum($\hbar = c = 1$), with

$$E = m_n + m_p + T = \sqrt{p^2 + m_n^2} + \sqrt{p^2 + m_p^2} \tag{1.28}$$

$$p^2 = \frac{E^2 - 2(m_n^2 + m_p^2) + (m_n^2 - m_p^2)^2}{4E^2} \tag{1.29}$$

where E is the total, relativistic energy in the c.m., the partial cross section has a pole at $p = i\gamma_d$, where γ_d is the scattering wave number, given by $\gamma_d^2 = -p^2$ from (1.29) for $T = -\epsilon_d$, or $E = m_n + m_p - \epsilon_d$, where ϵ_d is the binding energy. In terms of the asymptotic (free particle) n-p wave function $v_d(T)$ and the exact (interacting) n-p wave function $u_d(T)$, both of which implicitly depend on the neutron-proton separation r, the function $\rho_d(T_a, T_b)$ is defined as [19]

$$\rho_d(T_a, T_b) \equiv 2\int_0^\infty [v_d(T_a)v_d(T_b) - u_d(T_a)u_d(T_b)]dr \tag{1.30}$$

where ρ_d, v_d, u_d are ρ_t, v_t, u_t for the triplet and ρ_s, v_s, u_s for the singlet, and T_a and T_b are any two values of the c.m. kinetic energy. This definition satisfies (1.27) exactly for $T_a = 0$ and $T_b = T$. The wave function u_d, but not v_d, depends on the shape of the nuclear potential, and this shape dependence manifests itself as energy dependence of ρ_d.

As long as p^{-1} is much larger than the well size, the detailed shape of the nuclear potential can have only a small effect on the spectrum. The shape-independent approximation replaces $\rho_d(0,T)$ with the constant r_d,

$$\sigma_d \cong \frac{4\pi}{\left(\frac{1}{a_d} - \frac{1}{2}r_d p^2\right)^2 + p^2} \tag{1.31}$$

For the triplet only, r_t is taken as $r_t = \rho_t(0, -\epsilon_t)$, the "mixed effective range", given exactly as [19]

$$\rho_d(0, -\epsilon_d) = 2\frac{1}{\gamma_d}\left(1 - \frac{1}{a_d\gamma_d}\right) \tag{1.32}$$

A measured elastic cross section σ_p at p may be used to determine r_s as r_{sp}, the apparent singlet effective range at p, through (1.26), (1.31), and the parameters a_t, a_s, and r_t, thus

$$r_s = \frac{2}{p^2}\left(\frac{1}{a_s} + \sqrt{\frac{4\pi}{\sigma_{sp}} - p^2}\right) \tag{1.33}$$

where $\sigma_{sp} \equiv 4\sigma_p - 3\sigma_t(p)$ is the estimated singlet partial cross section and $\sigma_t(p)$ is the theoretical triplet partial cross section, obtained with (1.31).

In principle, $\rho_d(0,0) = lim_{T\to 0}\rho_d(0,T)$ approximates $\rho_d(0,T)$ better than $\rho_d(0,\epsilon_d)$ does, where the limit expresses the experimental condition that the variation with decreasing energy becomes smaller than the statistical error. Define Δr_d such that $\rho_d(0,0) = \rho_d(0,\epsilon_d) + \Delta r_d$. The condition $\Delta r_d \neq 0$ is referred to here as "zero-energy shape dependence." The (zero-energy) apparent singlet effective range $r_{s0} \equiv lim_{T\to 0} r_{sp}$ is an approximation to $\rho_s(0,0)$ with a systematic error $(\delta r_s)_{\Delta r_t}$, thus,

$$\rho_s(0,0) = r_{s0} + (\delta r_s)_{\Delta r_t} \tag{1.34}$$

$$(\delta r_s)_{\Delta r_t} \equiv \int_{r_t}^{r_t+\Delta r_t} dr_t \frac{\partial r_s}{\partial r_t} = \langle \frac{\partial r_s}{\partial r_t} \rangle \Delta r_t \tag{1.35}$$

$$\frac{\partial r_s}{\partial r_t} = -\frac{3\sigma_t^2\left(\frac{1}{a_t} - \frac{1}{2}r_t p^2\right)}{\sigma_s^2\left(\frac{1}{a_s} - \frac{1}{2}r_s p^2\right)} \tag{1.36}$$

The measurements and their uncertainties are:

$\sigma_0 \pm \delta\sigma_0$ the zero-energy elastic cross section

$a_c \pm \delta a_c$ the parahydrogen coherent scattering length

$\sigma_p \pm \delta\sigma_p$ the elastic cross section at c.m. momentum p.

The uncertainties $\delta\sigma_0$, δa_c, and $\delta\sigma_p$ are small and independent. Because its uncertainty is utterly negligible compared to the others, ϵ_t is taken as exact. The zero-energy (free proton) elastic cross section is given by (1.26), taking $p = 0$ in (1.27), thus

$$\sigma_0 = \pi(3a_t^2 + a_s^2) \tag{1.37}$$

The parahydrogen coherent scattering length is

$$a_c \equiv \frac{3}{2}a_t + \frac{1}{2}a_s \tag{1.38}$$

Because a_t and a_s are correlated, σ_0, a_c, and r_{s0} are taken as the fit variables, with

$$s \equiv \sqrt{\frac{1}{12}\left(\frac{\sigma_0}{\pi} - a^2\right)} \tag{1.39}$$

$$a_s = \frac{1}{2}a_c - 3s,\ \ a_t = \frac{1}{2}a_c + s. \tag{1.40}$$

Contributions from higher waves increase the cross section and decrease the apparent singlet effective range if not accounted for.

The fit parameter σ_0 is determined almost entirely by the lowest-energy data, and the fit parameter a_c almost entirely by the a_c data, so these are very nearly independent of T_{max}.

The shape-independent parameters are determined to be [43]

$$\begin{aligned}
\sigma_0 &= 20.4278 \pm 0.0078 \text{ b} && (1.41)\\
a_c &= -3.7406 \pm 0.0010 \text{ fm} && (1.42)\\
r_{s0} &= 2.750 \pm 0.018_{\mathrm{stat}} - 0.059_{\mathrm{syst}} \text{ fm} && (1.43)\\
a_t &= 5.4112 \pm 0.0015 \text{ fm} && (1.44)\\
a_s &= -23.7148 \pm 0.0043 \text{ fm} && (1.45)\\
\rho_t(0,-\epsilon_t) &= 1.7436 \pm 0.0019 \text{ fm} && (1.46)\\
\epsilon_s &= 66.26 \pm 0.05_{\mathrm{stat}} + 0.14_{\mathrm{syst}} \text{ keV} && (1.47)\\
\rho_t(0,0) &= 1.718 \pm 0.025 \text{ fm} && (1.48)\\
\rho_s(0,0) &= 2.696 \pm 0.059 \text{ fm} && (1.49)\\
\Delta r_t &= -0.025 \pm 0.025 \text{ fm} && (1.50)
\end{aligned}$$

The errors are statistical, representing standard deviations. The one-sided systematic error shown for r_{s0} represents a one-standard-deviation error in its approximation to $\rho_s(0,0)$. The one-sided systematic error on ϵ_s is propagated from the systematic error on r_{s0} , which is used instead of $\rho_s(0,\epsilon_s)$ in (1.32).

1.3 Previous Data

Figure 1.2 shows existing neutron-proton cross section data taken from the National Nuclear Data Center [27–36]. There are only a few data points between 100 and 500 keV, which disagree with each other and with the theoretical models. [25, 26] With current results, Δr_t is a measure of errors in the data rather than a measure of zero-energy shape dependence.

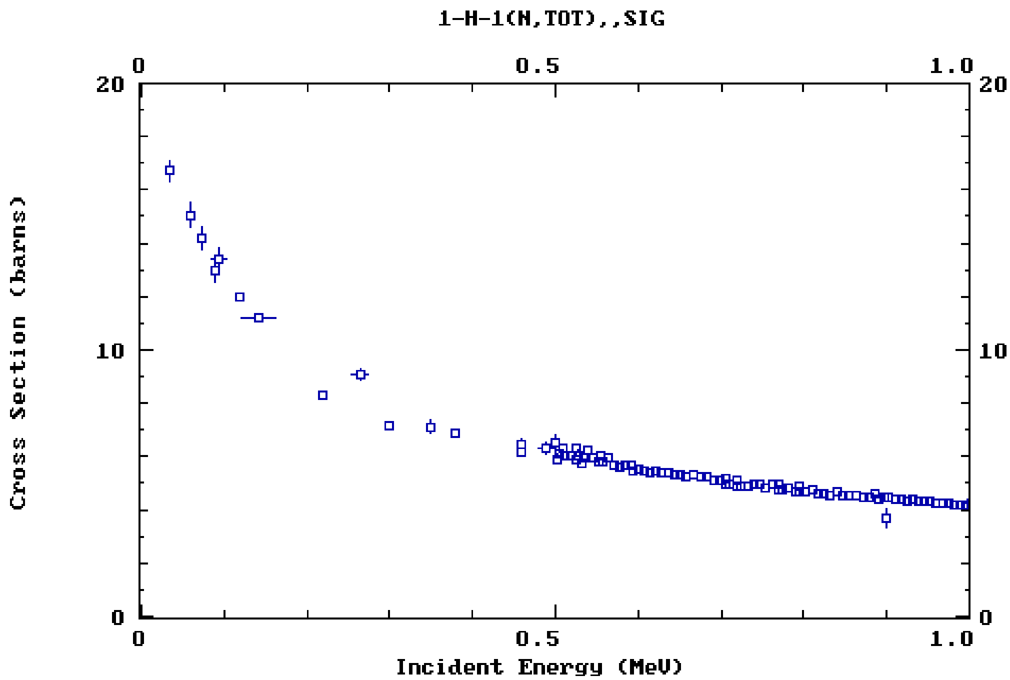

Figure 1.2: Existing data on the n-p cross sections from EXFOR on NNDC.

Figure 1.3 demonstrates the correlation between the fit values of $\rho_t(0,0)$ and $\rho_s(0,0)$.

At energies above 1.5 MeV, the shift in cross section is almost insensitive to either $\rho_t(0,0)$ or $\rho_s(0,0)$. While at energies below 1.5 MeV, there are too few and insufficiently precise data to break the correlation. Figure 1.4 emphasizes how poorly $\rho_t(0,0)$ and $\rho_s(0,0)$ are determined by the data available. It can hardly be decided whether the reference line at zero or one of the curves describes the data better. The maximum shift occurs at 130 keV in upper curve. Thus, $\rho_t(0,0)$ and $\rho_s(0,0)$ are most sensitive to a measurement at this energy. The sensitivity falls to half maximum at

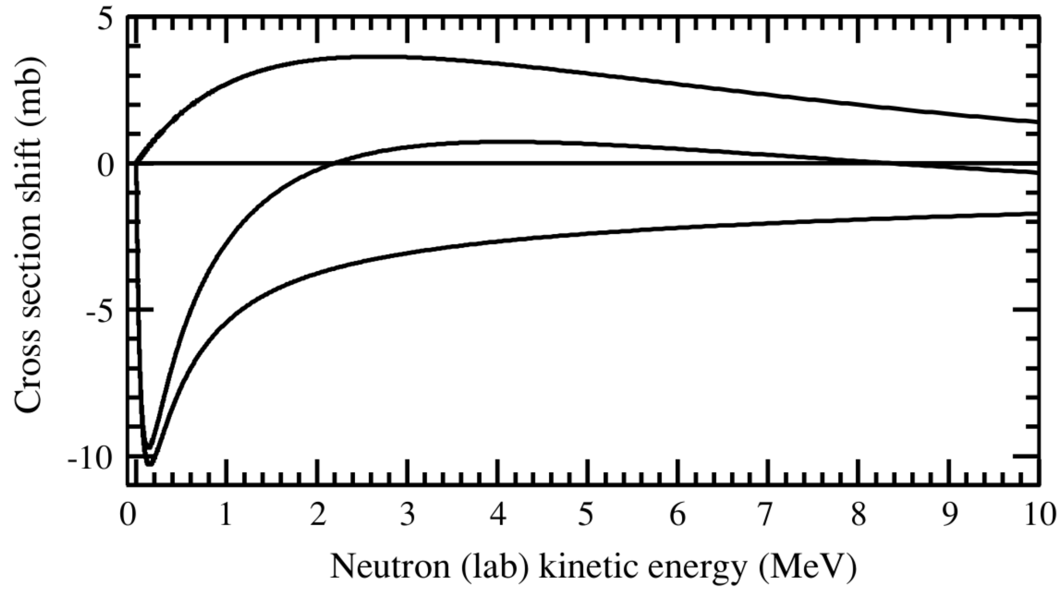

Figure 1.3: The effect on the calculated cross section of the correlation between $\rho_t(0,0)$ and $\rho_s(0,0)$. (line at zero) $r_t = \rho_t(0,0)$, $r_s = \rho_s(0,0)$ from (1.50); (upper curve) $r_t = \rho_t(0,0) + 0.025$ fm, $r_s = \rho_s(0,0)$; (middle curve) $r_t = \rho_t(0,0) + 0.025$ fm, $r_s = \rho_s(0,0) + 0.059$ fm; and (lower curve) $r_t = \rho_t(0,0)$, $r_s = \rho_s(0,0) + 0.059$ fm.

23 and 620 keV. But unfortunately, the useful data in this range are very sparse.

In order to overcome the correlation between $\rho_s(0,0)$ and $\rho_t(0,0)$, improved low-energy cross-section measurements between about 20 and 600 keV are needed. A single cross section with a precision of 0.4 mb near 130 keV would reduce the errors on $\rho_t(0,0)$ and Δr_t to about 0.001 fm. As it stands, Δr_t is more a measure of errors in the data than a measure of zero-energy shape dependence; it is insufficiently well determined to be of any use in a comparison with predictions from potential models.

The motivation for the present experiment is to allow comparison to predictions from nuclear potential models, the uncertainty on $\rho_t(0,0)$ and Δr_t must be reduced. As it is most sensitive at a neutron energy of 130 keV as stated above, the focus of this experiment is the energy range between half of its maximum value at 23 and 620 keV. A previous measurement has been carried out in the energy range from 150 to 800 keV, as shown in Figure 1.5 [44]. Although the result itself is a good breakthrough in this energy region, it still has insufficient precision due to several experiment limitations such as dead time correction, beam intensity normalization,

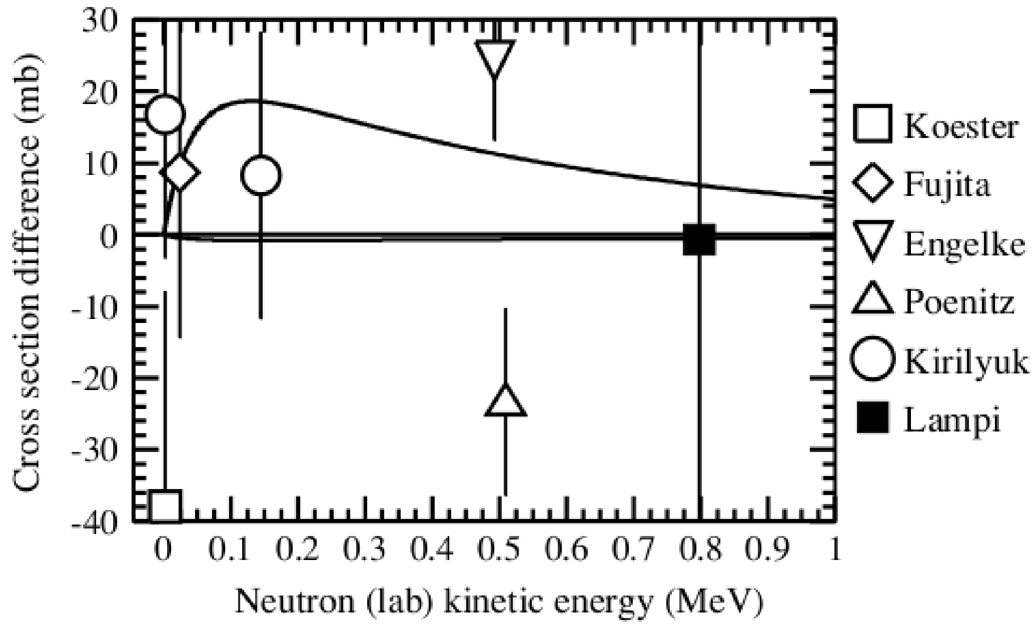

Figure 1.4: Cross-section differences. The cross section calculated with the parameters from (1.43)-(1.46) is subtracted from data and calculations made with other choices of parameters. The curves form the one-standard-deviation envelope for the cross section calculated with $\rho_t(0,0)$ and $\rho_s(0,0)$ from (1.50); (line at zero) Shape-independent parameters from (1.43)-(1.46); (upper curve) $r_t = \rho_t(0,0)0.025$ fm, $r_s = \rho_s(0,0)0.059$ fm; and (lower curve) $r_t = \rho_t(0,0) + 0.025$ fm, $r_s = \rho_s(0,0) + 0.059$ fm. The lower curve is below and barely separated from the line. Data: [30] (Koester), [20] (Fujita), [29] (Engelke), [34] (Poenitz), [28] (Kirilyuk), and [21] (Lampi). Off-scale data are omitted; these have error bars that would span the entire vertical range of the plot.

etc. As a result, there is a noticable systematic shift for carbon data as shown in Figure 1.6.

The goal is to get the cross section data over an extended range with sufficient precision by overcoming all the significant limitations in the previous experiment.

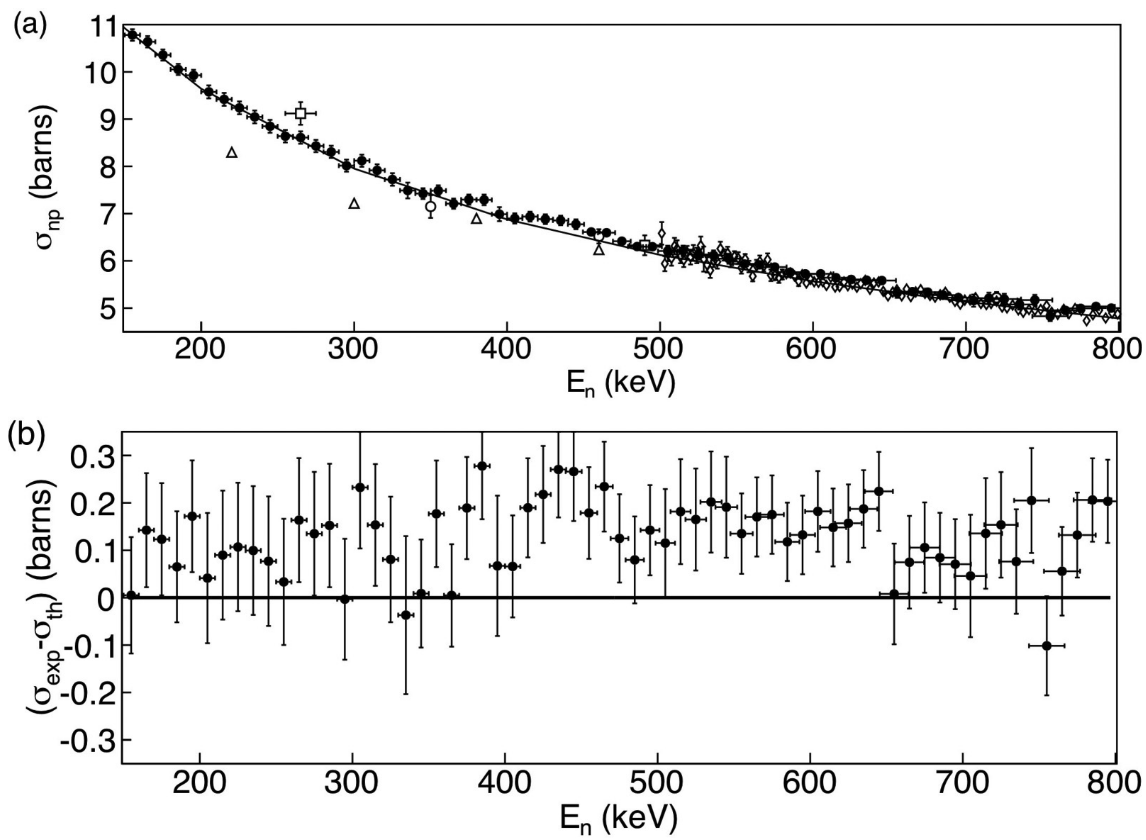

Figure 1.5: The n-p cross sections from previously published work [44].

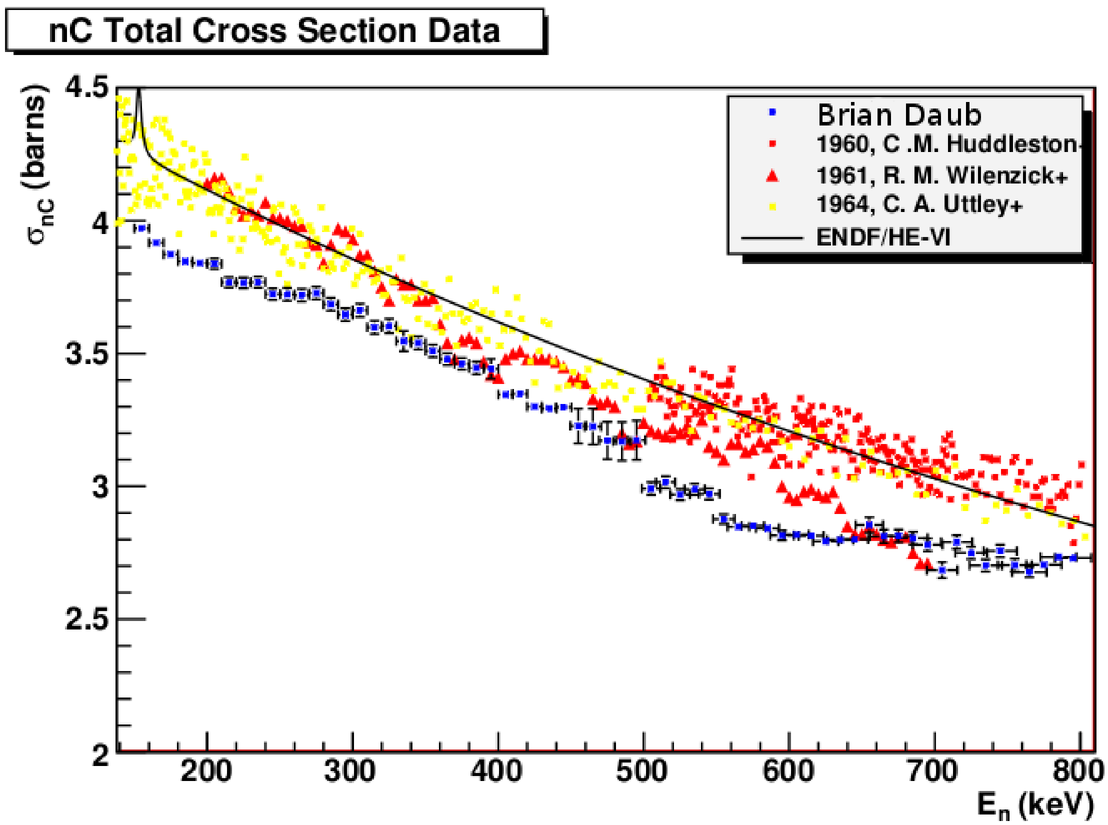

Figure 1.6: The n-C cross section results from Brian Daub's dissertation [45].

Chapter 2 Experiment Setup

2.1 Method

The attenuation method was used to measure the cross sections.

The scattering cross section is an effective area that quantifies the intrinsic rate a given event(s) occurs during the scattering of two particle species (in quantum mechanics, this also includes waves). Conventionally, one of the species is treated as a projectile (incident beam), and the other species is treated as a target (scattering center).

Intuitively, an event is said to have a cross section of σ if its rate is equal to the rate of collisions in an equivalent, idealized experiment where:

(1) The projectiles are replaced by inert point-like particles, and

(2) The targets are replaced by inert and inpenetratable disks of area σ (and hence the name "cross section"), with all other experimental parameters kept the same (assuming the target sample is sufficiently thin). Mathematically, this is described as:

$$W = N \cdot I \cdot \sigma \tag{2.1}$$

where W is the rate at which the event occurs (SI units: s^{-1}), N is the number of target particles within reach of the incident beam (dimensionless), I is the particle flux (or intensity) of the incident beam (SI units: $m^{-2}\ s^{-1}$), and σ is the cross section of this event (SI units: m^2).

Essentially, the cross section is a measure of the rate that controls for the experimental parameters N and I.

Suppose an incident beam with intensity I_i going through a sample of thickness $d\tau$, then N in unit area can be written as

$$N_{\text{unit area}} = \frac{d\tau \cdot \rho}{A} \cdot N_A \tag{2.2}$$

where A is the atomic mass. N_A is Avogadro's constant.

By definition, the output beam intensity I_o can be expressed as a function of the sample material cross section σ.

$$I_o = I_i - W = I_i \cdot \left(1 - \frac{\rho \cdot N_A}{A} \cdot d\tau \cdot \sigma\right) \tag{2.3}$$

Integrating over thickness $d\tau$,

$$I_o = I_i \cdot e^{-\frac{\rho \cdot N_A}{A} \cdot \sigma \cdot \tau}. \tag{2.4}$$

Then, the cross section σ can be calculated as:

$$\sigma = \frac{A}{\rho \cdot N_A \cdot \tau} \cdot \ln \frac{I_i}{I_o}. \tag{2.5}$$

In the current experiment, I_i and I_o cannot be measured simultaneously. Instead, with all the setups remaining the same, the sample is switched in and out, so the measurement of intensity I_i can be achieved by taking the sample out of beam; similarly, I_o is measured when sample is in the beam. Then the cross section is represented by measurable variables and can be written as

$$\sigma = \frac{\alpha}{\tau} \cdot \ln \frac{Y_{\text{Out}}}{Y_{\text{in}}}, \tag{2.6}$$

where $\alpha = A/(N_A \cdot \rho)$, Y_{in} and Y_{out} are normalized yields when the sample is in and out, respectively.

2.2 Van de Graaff Accelerator

A Van de Graaff generator is an electrostatic generator which uses a moving belt to accumulate electric charge on a hollow metal globe on the top of an insulated column, creating very high electric potentials. It produces very high voltage direct current (DC) electricity at low current levels. It was invented by American physicist Robert J. Van de Graaff in 1929. The potential difference achieved in modern Van de Graaff generators can exceed 5 megavolts.

The type CN Van de Graaff accelerator in University of Kentucky is used to generate the required proton beam. Gaseous hydrogen is ionized by a radio-frequency electric field. A DC beam is then produced by accelerating the positive plasma that leaks out of the ion source, then the ions are focused together into the beam. To pulse the beam, a radio-frequency sweeping magnetic field is produced, which causes the focused beam to travel in an ellipse. This ellipse lands on the chopping apperature, so that the beam only passes through the chopper once per rotation. Since the period of the sweep magnet is 1.875 MHz, the beam pulsing has this same period, which results in 533 ns between beam pulses. The pulsing is further refined by a bunching magnet, which squeezes the beam in time, so that all the protons arrive at the neutron production target within one nanosecond.

Solid lithium fluoride targets were used to produce neutrons via the ^{7}Li(p, n)^{7}Be reaction, which has a Q value of 1.644 MeV [37, 38]. The LiF targets were produced by evaporating LiF onto a tantalum disc, allowing them to be made with varying thickness. So, while the flux at a given neutron energy will be approximately fixed, the range of the energy spectrum will vary with the target thickness. A thick target will produce a wide range of neutron energies, while a thin target will produce a smaller energy range. Since the experiment has a wide energy span of 2 MeV, both 20 μm and 10 μm LiF targets were used in this experiment to produce $\sim$50 keV wide neutron beams in high and low beam energies, respectively.

The typical beam current is 1.5 - 2 μA, depending on the energy. The trigger rate at this intensity is 1 - 2 kHz.

2.3 Detectors

2.3.1 Neutron Detector

BC-501A is a premium deuterated liquid scintillator intended for applications involving neutron detection in the presence of gamma radiation. The scintillator is 5.1 cm diameter by 5.1 cm thick cylindrical shaped. BC-501A is a popular scintillator and is formulated to yield excellent PSD (pulse-shape discrimination) properties for neutron-γ discrimination [39]. It is in an ready-to-use version that is encapsulated in metal cells and is equipped with a photomultiplier and a voltage divider. Its characteristics are shown in Table 2.1. In the last row, P is the proton energy in MeV, E is the electron energy in MeV that gives the same light output.

Table 2.1: Properties of BC-501A. [40–42]

Name	Value
Light Output	78% Anthracene
Wavelength of Maximum Emission	425 nm
No. of D Atoms	$4.82 \times 10^{22}/cc$
No. of C Atoms	$3.98 \times 10^{22}/cc$
Ratio D:C Atoms	1.212
No. of Electrons	$2.87 \times 10^{22}/cc$
Mean Decay Times	3.16, 32.3 & 270ns
Mean Life Time from solvent to solute	1.66 ns
Photoelectrons using Burle 8575 phototube	1.7/keVee
Ratio, Alpha:Beta, fast	0.073
Ratio, Alpha:Beta, slow	0.098
Response to protons (MeV)	$E = 0.83P + 282(e^{-0.25P^{0.93}} - 1)$

2.3.2 Neutron Monitor

The long counter was used in this experiment as the neutron monitor. Long counters are well known for their flat response function over a wide neutron energy range. Generally, they have a high efficiency, they are insensitive to photons and their directionality as well as their good stability make them ideal neutron detectors for measurements of parallel neutron fields, from a few keVs up to a few MeVs. A long counter consists of a cylindrical thermal neutron detector located in the center of a cylindrical hydrogenated moderator. The moderator container generally includes an annulus of a thermal neutron absorber.

The long counter has been and remains an essential tool for quantifying sources of neutrons in essentially all neutron metrology laboratories. It derives its utility from its nearly constant counting efficiency over a wide neutron energy range. Since its development in 1947 by Hanson and McKibben [22], the long counter, more than any other instrument, has been used to calibrate unknown isotopic neutron sources against various national neutron standards and to quantify neutron production in targets of various accelerators for producing monoenergetic neutrons via common reactions such as d-d, d-T, p-T, and p-^{7}Li. Almost every laboratory involved in neutron physics and neutron dosimetry has a long counter on its list of essential equipment. Discussions on long counters, including later variants of the initial design, can be found in standard reference books [23, 24].

Since its sensitivity is approximately uniform at our interested neutron energy range, we chose it to be our neutron flux monitor for beam intensity normalization.

2.3.3 Germanium Detector

Germanium detectors are mostly used for gamma spectroscopy in nuclear physics. While silicon detectors cannot be thicker than a few millimeters, germanium can have a depleted, sensitive thickness of centimeters, and therefore can be used as a detector for gamma rays up to few MeV. These detectors are also called high-purity germanium detectors (HPGe) or hyperpure germanium detectors. Before current purification techniques were refined, germanium crystals could not be produced with purity sufficient to enable their use as spectroscopy detectors. Impurities in the crystals trap electrons and holes, ruining the performance of the detectors. Consequently germanium crystals were doped with lithium ions (Ge(Li)), in order to produce an intrinsic region in which the electrons and holes would be able to reach the contacts and produce a signal.

2.4 Samples

Three CH_2 and three carbon samples with different thicknesses are used in these experiments. The n-p cross section can then be extracted by subtracting the n-C cross section from the n-CH_2 cross section. An 2.54 cm thick sulfur sample is also used as the calibration sample due to its multiple resonance peaks below 1 MeV.

The characteristics of carbon and CH_2 samples shown in Table 2.2 and Table 2.3 were measured by a caliper and a high resolution balance.

Table 2.2: Detailed carbon sample attributes.

Sample	Length(mm)	Diameter(mm)	Mass(g)	$\rho(g/cm^3)$
C 3.1	30.98 (0.01)	49.09 (0.03)	93.96 (0.01)	1.602 (0.002)
C 4.6	46.41 (0.01)	49.165 (0.025)	141.27 (0.01)	1.607 (0.002)
C 6.1	61.00 (0.01)	49.165 (0.015)	187.48 (0.01)	1.619 (0.001)
Average				1.609 (0.003)

Table 2.3: Detailed CH_2 sample attributes.

Sample	Thickness(mm) ($\Delta\tau$)	Length(mm) (ΔL)	Width(mm) (ΔW)	Mass(g) (ΔM)	$\rho(g/cm^3)$ ($\Delta\rho$)
CH_2 1	10.145 (0.045)	76.195 (0.005)	50.965 (0.025)	37.44 (0.01)	0.9504 (0.0042)
CH_2 2	20.38 (0.02)	76.985 (0.075)	50.96 (0.07)	76.11 (0.01)	0.9519 (0.0019)
CH_2 3	30.5 (0.02)	77.015 (0.055)	50.885 (0.045)	114.02 (0.01)	0.9539 (0.0013)
Average					0.9521 (0.0048)

In order to achieve optimal overall statistical error, optimal time allocation for each of our samples should be identified. Since the theoretical cross section distributions are known for all samples at the interested energy range, the first thought is that the best time allocation should result in similar total counts for each of the samples. While that is generally true, additional consideration should be made for the thinnest sample. It's not only the total counts through the sample, but also the total counts of sample-out that is important. So for an imprecise but a good approximation, a time distribution that equalizes the minimum yield of both through counts and scattered counts is used for each sample. Using blank (sample-out) as a time reference, suppose we are allocating a unit time to sample-in and out, using f as the fraction of time for sample-in, the uncertainty of σ is given by:

$$\delta_\sigma(f) = \frac{1}{\rho^2\tau^2 I_0 T}\left(\frac{1}{1-f} + \frac{1}{\mathrm{Min}\left(1-e^{-\sigma\rho\tau}, e^{-\sigma\rho\tau}\right) f}\right) \tag{2.7}$$

where ρ is the sample density, τ is the sample thickness, σ is the sample cross section.

Finding the optimal f simply means to solve it as a differential equation of variable f,

$$\frac{\partial}{\partial f}\delta_\sigma(f) = 0 \tag{2.8}$$

The result is the best time ratio for a given sample at a given beam energy relative to the blank (sample-out). By repeating the same calculation for all samples, the results for several incident neutron beam energies are shown in Table 2.4.

Table 2.4: Sample dwelling time allocation.

Name	E_n		
	200keV(s)	800keV(s)	1.8MeV(s)
Blank	163	221	269
CH_2 1	283	327	487
CH_2 2	490	406	388
CH_2 3	850	551	466
C 3.1	313	387	385
C 4.6	434	511	446
C 6.1	601	677	527
Sulfur	267	320	432

The sample-switching-wheel layouts are: 1. Blank, for data collection preparation; 2. Blank; 3. CH_2 2cm; 4. CH_2 1cm; 5. Blank; 6. CH_2 3cm; 7. Carbon 3.1cm; 8. Blank; 9. Carbon 6.1cm; 10. Carbon 4.6cm; 11. Blank; 12. Sulfur. When samples are in position, the wheel controller will send out analog signals with different amplitudes indicate the sample ID. During sample switching times, the controller will also send out a logic signal indicating its busy status, which can be used to veto the data collection process.

The first blank sample is not data related, it gives some preparation time for data collection to begin. All the other Blank samples are there so that non-blank samples would have an adjacent blank sample to normalize to. Normalization precision can be improved by this configuration, which will be propagated to the final overall precision. Because the neutron beam created by accelerator is not uniform over time, the normalization only makes sense when the data acquisition conditions do not change over time, i.e. electronics and detectors must be stable until both sample-in and sample-out data collections are finished. Since the stability worsens over time, to make the sample-in and sample-out close to each other will reduce the time difference to at most 20 minutes, minimizing the potential electronics stability variations. As a result, the normalization uncertainties are negligible compared to other major contributors such as background and sample density variations.

2.5 Measurement Area Setup

After the neutrons are produced with LiF target, they enter into the experiment area; the dimensions of the layout are shown in Figure 2.1.

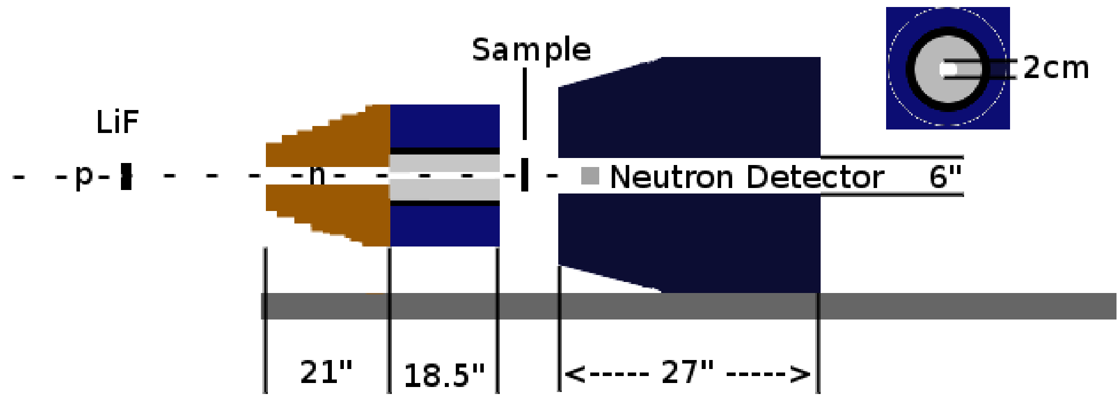

Figure 2.1: Measurement area configurations. The drawing on the upper right corner is the back view of the second shield. The outside material is wax, and the black ring is made of lead. Inside the black ring is another layer of wax with a 2 cm hole at the center.

The total flight path from neutron creation (LiF target position) to the neutron detector is 301.5 cm and 174 cm for the Sept. 2014 and Feb. 2015 runs, respectively. Figure 2.2 shows a photograph of the experiment area for the Sept. 2014 run.

The first two shilding are used to collimate the neutron beam, the smallest apature of 2 cm in the second collimator defines the incident beam on samples. An automatic sample-switching wheel controlled by a micro-controller was used to minimize the time needed to switch the samples, this also reduced the possible time related errors caused by electronics such as detector gain shift. The samples are aligned with the beam collimator within 1/8" so that all the beam coming out of the collimator will hit the sample. At the end of the setup is the deuterated BC-501A neutron detector. The detector is also shielded by a iron shield to prevent it from receiving events from outside of the beam line.

Table 2.5 shows more detailed measurements of all the shieldings in the setup.

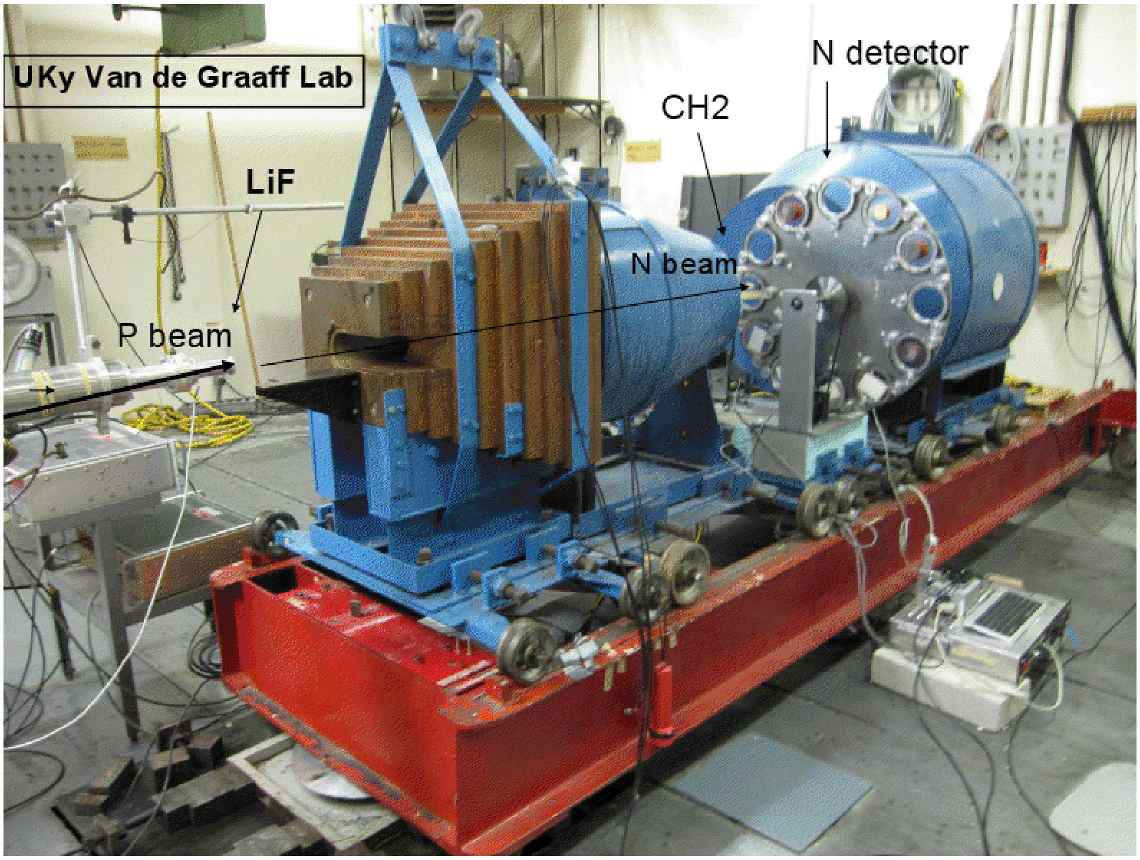

Figure 2.2: Experiment Setup in UK Van de Graaff lab.

Table 2.5: Shielding dimensions

Name	Material	Length (inch)	Attribute	Value (inch)
Shield 1	Copper	21	Height/Width (front)	12
			Height/Width (back)	24
			Center Hole OD	3
Shield 2	Wax (outer)	18.5	Height/Width	24
	Lead		OD	10
	Wax (inner)		OD	7.5
			Center Hole OD	2 cm
Shield 2	Iron	43	OD (front)	27.5
	Iron		OD (back)	40
	Wax		OD	16.25
	Lead		OD	10.5
			Center Hole OD	6

2.6 Electronics

The electronics are mostly set up in NIM bins and CAMAC crates. NIM modules are used to build the logic and make the signals ready to be collected by data acquisition system (DAQ), as explained in the next section. There are 14 signals to collect in total, including 3 analog to digital converter (ADC) signals, 3 time to ditital converter (TDC) signals and 8 scalers.

The signal sources in the measurement area are: neutron detector, wheel position, wheel valid, long counter, beam pickoff and charge integrator signals. Among them, the neutron detector signal is the major signal of the focus, because its clearness directly impacts the final precision of the result. And it has been identified that the sample wheel power system was the source of interruption that limits our previous results. The symptom is that there are periodical (20 kilohertz) 20 - 100 mV signals mixed with neutron detector signals. By choosing the appropriate power supply, this symptom was eliminated.

When the signals are transferred into the control room, they are feed into the electronics; Figure 2.3 shows a complete diagram of our Sept. 2014 run, where the module details are shown in Table 2.6.

Table 2.6: Details of all the modules used in electronics diagram.

Symbol	Name	Model	Vendor
ND	Neutron Detector	BC-501A	Saint-Gobain Crystals
AMP	Timing Amplifier/Fast AMP	574/535	ORTEC
ATTEN	Quad Rotary Attenuator	804	Phillips Scientific
COIN	Quad Four Fold Logic Unit	754/755	Phillips Scientific
LGFI/FO	Quad Linear Gate Fan-In/Out	744	Phillips Scientific
FI/FO	Linear Fan-In/Fan-Out	428F	LeCroy
CFD	Quad CFD	934	LeCroy
LI/LO	Logic Fan-In/Fan-Out	429A	LeCroy
LG	Linear Gate/Mux	7445	Phillips Scientific
DISC	Quad Discriminator	821	LeCroy
ADC	Analog to Digital Converter	4300B	LeCroy
TDC	Time to Digital Converter	4303	LeCroy
Scal	SCALER	2551	LeCroy

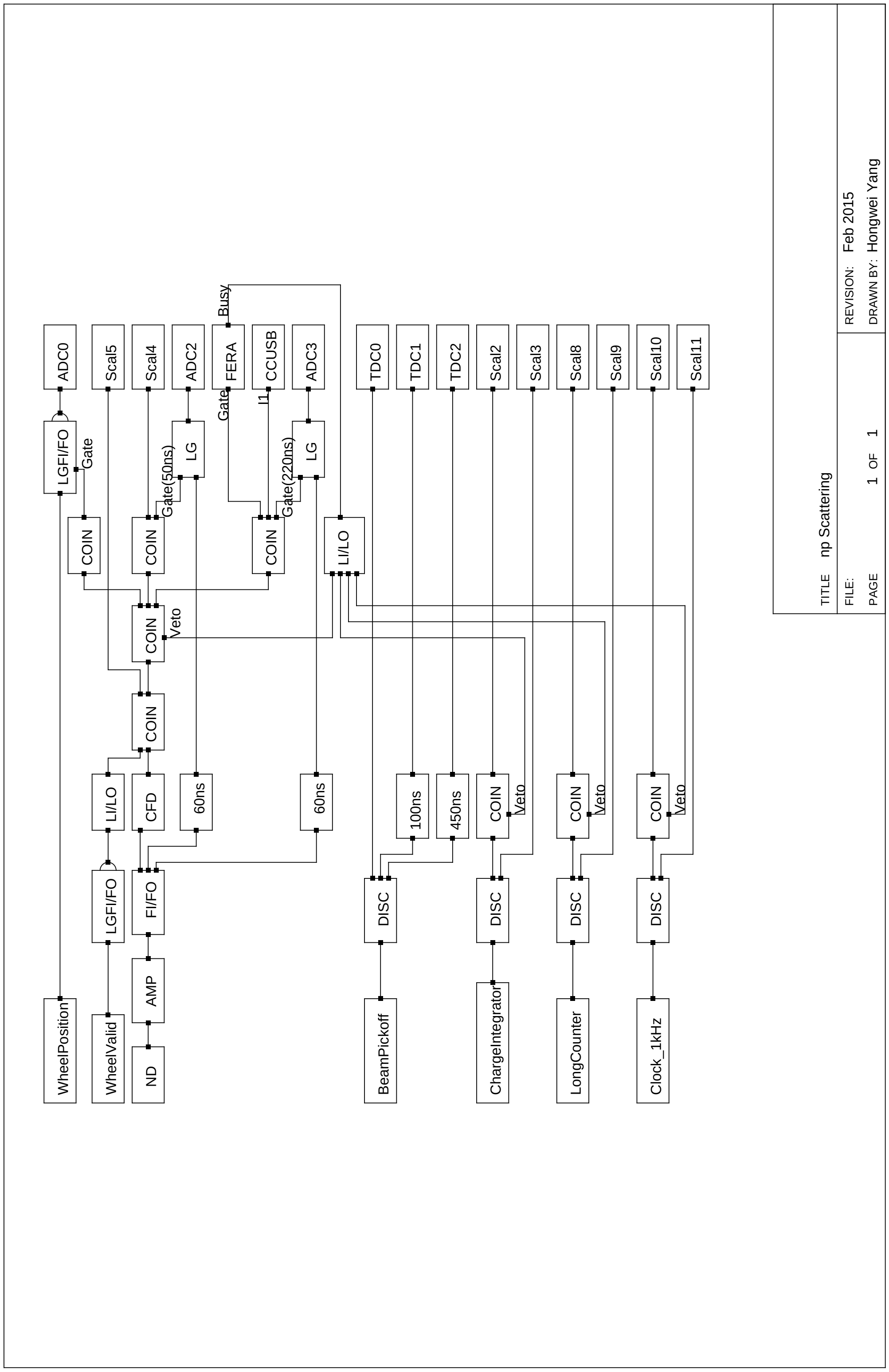

Figure 2.3: Electronics setup for n-p Sept. 2014 run.

2.7 Data Acquisition System

2.7.1 FERA/FERET

FERA (Fast Encoding and Readout ADC) and Fast Encoding and Readout TDC (FERET) systems consist of modules designed for fast conversion of analog information, either charge or time intervals, into a digital format. They also provide fast readout to a storage memory module or to a computer for further processing. The system modularity allows small as well as large multi-channel ADCs or time digitizing (TDC) systems to be configured and also allows simple memory expansion. These units can be used with other modules to configure energy-based or time-based triggers tailored for specific applications.

The heart of the system is the LeCroy Model 4300B, a charge-sensitive analog-to-digital converter. Other elements in the system include the Model 4301, a utility module for distribution of common signals and regeneration of signals for multiple 4300Bs; the Model 4302, a dual-port fast access memory module; and the Model 4303, which converts time intervals into charge signals to be measured by the Model 4300B.

The features of FERA system are:

(1) Constant Short Conversion Time for ADC - The time for conversion is 4.8 μs at 10 bits and 8.5 μs at 11 bits. This is independent of the number of channels or modules making up a system.

(2) Fast Data Readout - A readout speed of 10 MB/s, associated with pedestal subtraction and zero suppression capabilities, allows a uniquely fast data acquisition rate both for charge and time interval measurements.

(3) High Resolution - The least count resolution in charge is 0.25 pC. It is adjustable in time from 50 psec to 500 psec.

(4) System Flexibility - Due to its modular nature, a system can be easily expanded and adapted to measure charge or time intervals or both, and can also be easily interfaced to CAMAC, FASTBUS or GPIB.

(5) Trigger Capability - The FERA/FERET systems have been designed so that

the digitized charge or time information can be given as an input to second-level trigger processors built around the ECL Data Handler Modules.

The FERA system was configured to use the Model 4300B, Model 4301 FERA Driver, Model 4303 Time-to-Charge Converter along with CMC 203.

The 4301 FERA Driver is a utility module which distributes signals common to the system, such as gate, fast clear, test and handshake signals, via the command bus. It also receives data from the fast data bus, which collects data from all Model 4300Bs in the system, and translates it for transmission to the memory module or to the ECL logic units.

Then 4300B is used to convert charge into 11 bits data. After conversion, the digitized data may be automatically corrected with values contained in the programmable internal pedestal memory.

Digitized data is available first on the front-panel ECL port and subsequently on the CAMAC dataway. The ECL port readout is optional. All zero or zero-and-overflow data words may be suppressed to provide data compression. The compression procedure takes 2.5 μs irrespective of the number of channels or modules in a system.

The front-panel bus system includes the protocol necessary to allow high-speed sequential readout to the LeCroy series of ECL Data Handler Modules and to the Model 4302, Dual Port Fast Memory.

Specifications of these models are shown in Table 2.7 and Table 2.8.

Table 2.7: Model 4303 TDC Specfication.

Name	Value
Signal Inputs	16 inputs in 17 x 2-pin connector
Three 2-pin connectors	100 ohm
Input Sensing	Time, common start or common stop
Analog Outputs	Current source
Gate	Used as input to 4300B
Gate Width	set by front-panel potentiometer
Typical Range	100 ns to 1 μs
Sensitivity	50 ps to 500 ps adjustable

Table 2.8: Model 4300B ADC Specfication

Name	Value
Analog Inputs	16
Connector	17 x 2-pin front-panel connector
Input Sensing	Charge (current integrating)
Impedance	50 ohm ±5%
Protection	±25 V for 1 μs transients
Maximum current for linear response	-30 mA
Resolution	11 bits
Conversion Time	8.5 μs
Typical Range	480 pC minus ADC pedestal
Sensitivity	0.25 pC ±3%
Typical Integral Linearity	±0.5 pC
Typical Differential Linearity: ±10%	
Residual Pedestal	1 pC 13 pC for gate width from 50 to 500 ns
Pedestal/Gate Width Coefficient	±3 pC/μs
Operating Temperature	0^o to 40^oC
Typical Temperature Coefficient	(-0.05% of reading ±0.1 count)/^{o}C
Long Term Stability	±(0.25% of reading + 0.5 pC)/week

Chapter 3 Data Acquisition

As shown in data acquisition system section, the data was collected by a FERA system through a USB cable. The FERA modules were driven by software based on the KMAX framework. In comparison to the previously used XSYS acquisition system, the event dead-time was effectively reduced from 160 μs to less than 15 μs. The data were written in plain '.txt' file, where one row representing one event. It has all the event information such as ADC, TDC and associated scaler data.

Once the data are collected, several short scripts were used to create data trees from these raw '.txt' files under framework of ROOT. The data processing can start afterwards.

3.1 Raw Data

As shown in the electronics setup section 2.6, there are three types of data been recorded: ADC, TDC and scaler counts.

ADC has three signals, NDLong, NDShort, and Wheel position; example spectra are shown in Figure 3.1, Figure 3.2, and Figure 3.3, respectively.

NDLong records the charge integral of the full event pulse from the neutron detector; the gate width is set to be 400 ns, which is long enough to enclose the neutron event from the highest energy.

NDShort is a short-gated version of the same event; it only records the 'head' of the pulse, the gate is usually 30 - 80 ns wide, depending on the neutron beam energy, where a shorter gate serves smaller energies and vice versa.

NDShort and NDLong are used to distinguish neutron events from γ-ray events using the pulse-shape discrimination (PSD) technique, the detail of PSD will be disscussed in the following chapter.

The wheel position signal identifies which sample is in the beam line.

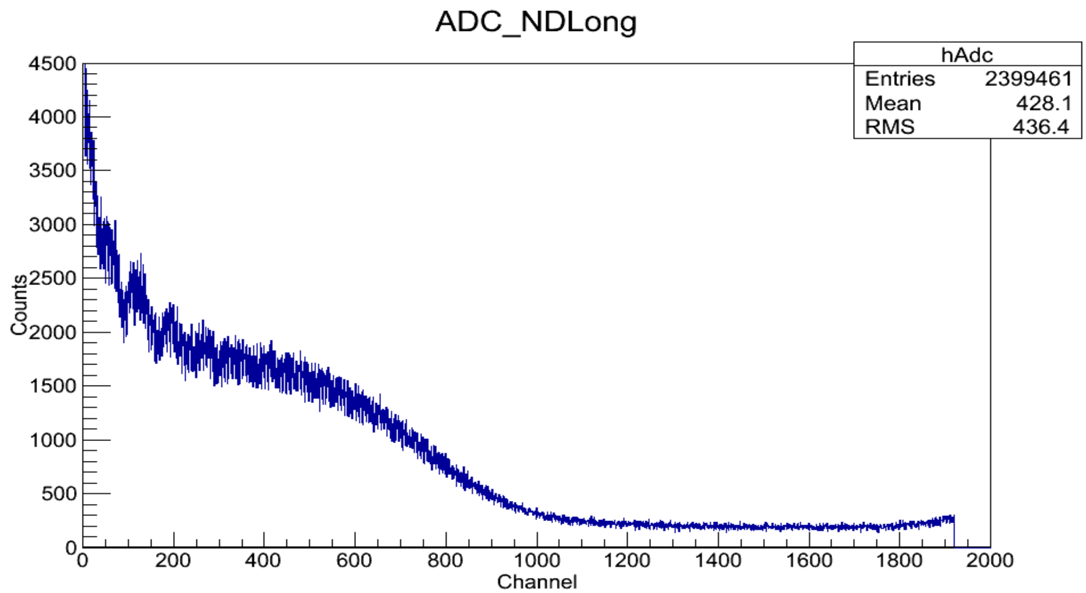

Figure 3.1: An example spectrum of long-gated ADC from run #320 for all samples. Incident neutron energy is 580 - 630 keV, trigger rate is 800/s, no signal attenuation is added. More information will be extracted in data analysis section.

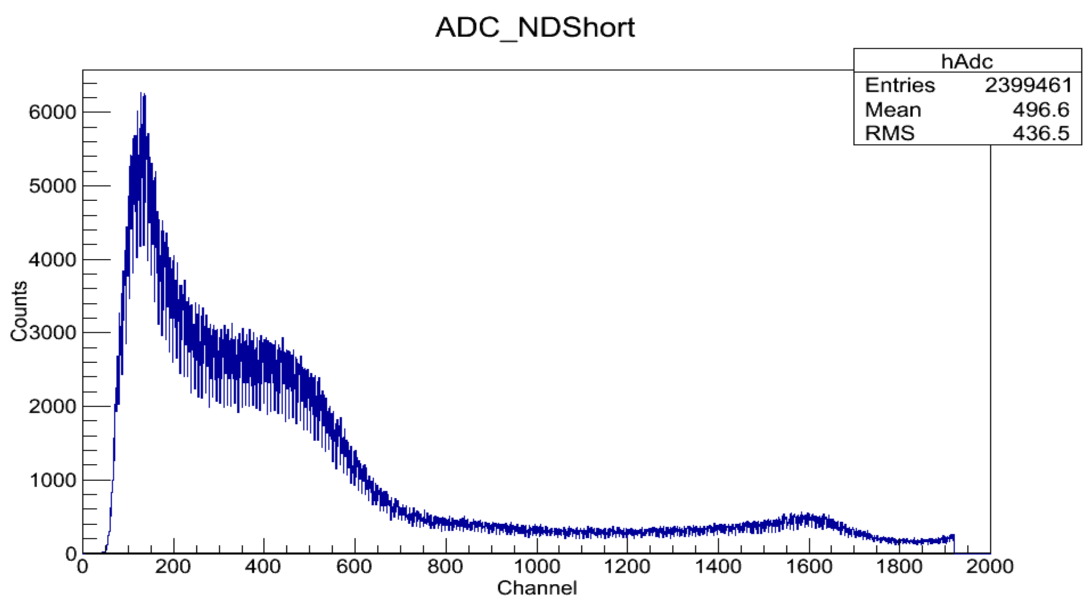

Figure 3.2: An example spectrum of short-gated ADC from run #320.

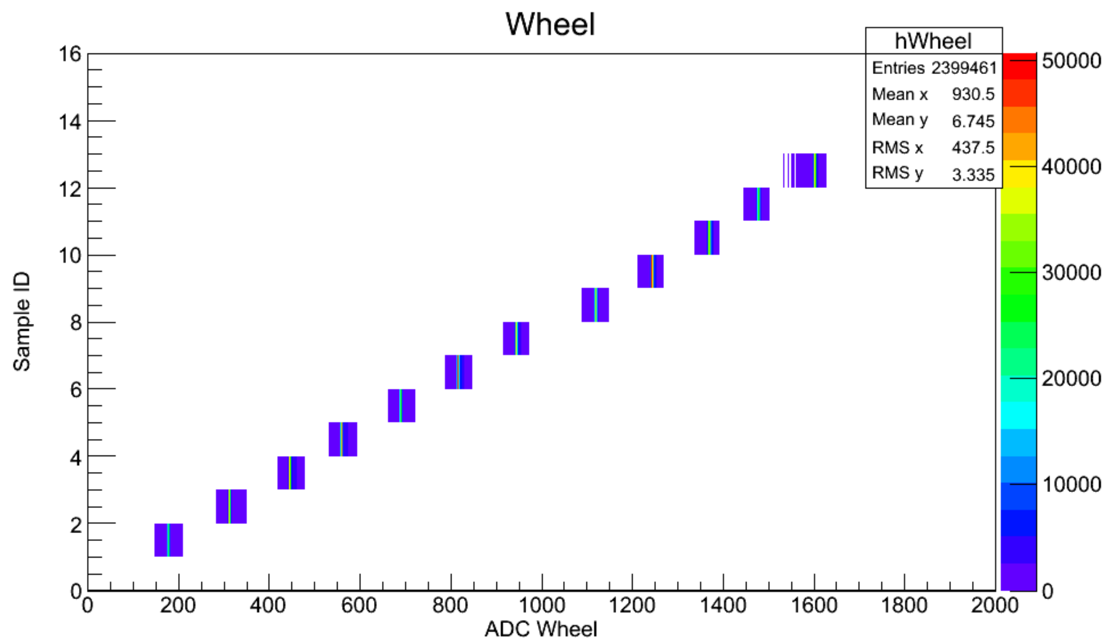

Figure 3.3: Wheel position signal.

The TDC (Figure 3.4) is exclusively used to record time-of-flight (TOF) information. In order to record only the events that triggers, it is operating in common stop mode. The event triggers mark the starting point, the stop point is the next beam pickoff. This configuration requires that the beam must be stable so that there is always a beam pickoff expected to come in time for every trigger. For technical reasons, the TDC module has limitations on the total time it can record (250 ns) when operating at high resolution (0.25 ns per channel) mode. As the longest TOF in this experiment is 300 - 400 ns at low energies, another two delayed triggers were also recorded in order to replay the whole TOF spectrum. Through TOF, the corresponding energy of the incident neutron beam can be calculated for each event.

The scaler records counts from several sources, such as charge-integral, long counter counts, raw trigger events, recorded trigger events (raw trigger events vetoed by FERA busy signal), etc.

Charge-integral: The integral of charge on the LiF target, this charge is brought in by the proton beam when it hits LiF to create neutrons. Since the neutron production is proportional to the proton intensity, the total charge can be used to normalize the

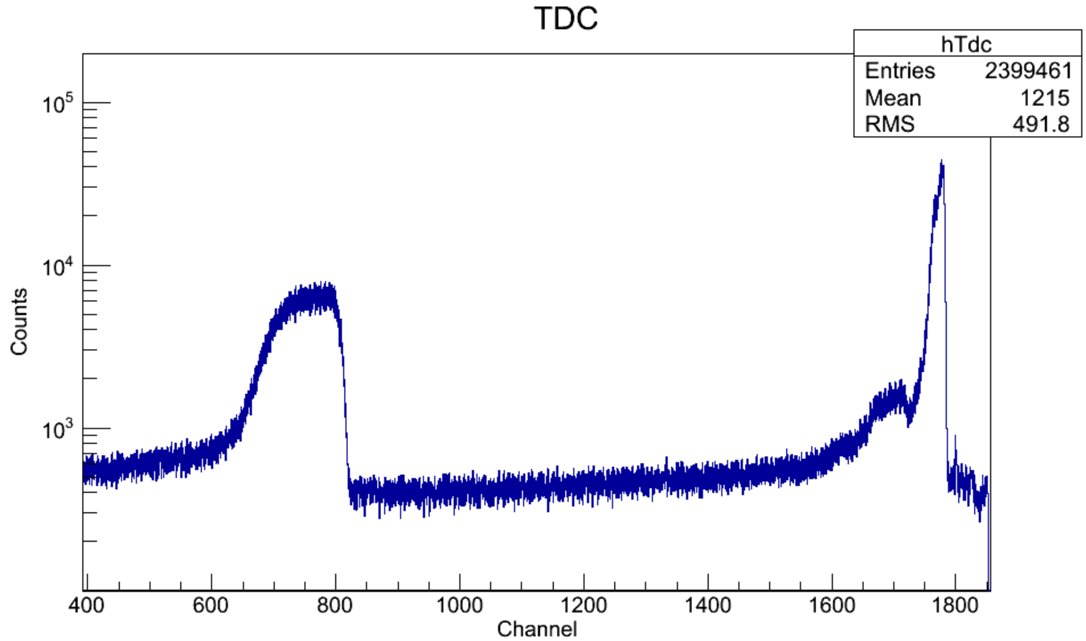

Figure 3.4: An example TDC spectrum from run #320. The flat peak in channel 600 - 800 is the neutron event region; the sharper peak around channel 1750 is the γ flash created during ^{7}Li(p, n)^{7}Be neutron creation. The TDC is operating at common stop mode, resulting in the high channels corresponding to events earlier in time.

neutron beam intensity. The sensitivity is adjusted to be 100 Hz/μA. The proton beam intensity is usually around 1 - 2 μA.

Chapter 4 Data Analysis

4.1 Analysis Overview

There are totally five analysis stages involved to obtain the final cross section.

Firstly, both ADC and TDC calibrations are needed. An ADC calibration tells the event energy to ADC channel correspondence, then the gain/attenuation factor in the amplifier/attenuator can be appropriately adjusted so that the neutron events with the maximum energy are within the ADC converting range. A TDC calibration is used to reproduce the precise time-of-flight (TOF) information for the incoming neutron beam; then the energy can be calculated from the TOF.

Secondly, a variety of cuts can then be applied on the spectrum; the purpose is to extract the 'net' neutron yields within the interested energy range. These cuts include ADC, TDC and PSD (neutron-γ pulse-shape discrimination), where the ADC cuts filter out the very low-energy events and high-energy cosmic rays. The very low-energy events are mixed with detector dark currents and γ rays; this is due to the detector characteristics, and it is the main factor that limits the ability to go to any lower energy region. TDC cuts filter out the events that are coming at the 'wrong' times, which are obviously beyond the interest range. PSD cuts finally separate out neutron events from γ ray events.

Then, after all the cuts above are applied, there are still events coming at the 'right' time, with reasonable energy, but still not coming directly from the samples. These events also need to be filtered out. As with current perception, there are two types sources making these events. One source is the random background events that are happening anytime anywhere; these event are easier to find, because if looking at the spectrum from TDC module, after applying ADC and PSD cuts, these backgrounds are uniformly distributed over time. By making a linear fit from outside of the major neutron arriving region, these events can be extrapolated for the region of interest. Another source is the events related with the beam itself. These events are not random. They are also neutron events coming from the beam, but they just missed the sample and, by chance, reflected back into the detector. These events cannot be filtered out from only applying cuts on spectrum, but they can be estimated by using Monte Carlo method. Several lab environment simulations based upon the Geant4 code are presented in the following sections.

After the above treatment for a single sample was done, the same process was repeated for all the other samples in a single run. Then, all the yields from different samples were normalized. Not only the beam condition, but also the electronics conditions will be slightly different over time, as discussed in the sample layout section above. All samples are normalized to their adjacent blank sample. The normalization process is done by using both the charge integrator and monitored neutron counts in the long counter.

Finally, the resulting counts are considered to be the 'net' neutron yields. These yields were used to calculate sample cross sections with appropriate neutron energy bins.

4.2 Calibrations

4.2.1 ADC Calibration

^{241}Am was used to calibrate the ADC, as shown in Figure 4.1. The 59-keV peak is centered near channel 800.

In order to scale the spectrum, an amplifier (ORTEC AMP Model 574) and an attenuator (Phillips Scientific Model 804) are used before the signal went into the ADC. Since the detector signal induced by a 59 keV γ ray is equivalent to $\sim$300 keV neutron energy, the gain/attenuator factor for ADC signals can then be adjusted according to the neutron beam energy in use.

The operating voltage of the neutron detector was choosen to be -2300 V. Because detector responses tend to become non-linear as operating voltage goes higher. This is the maximum voltage that the detector can still respond linearly to incoming events.

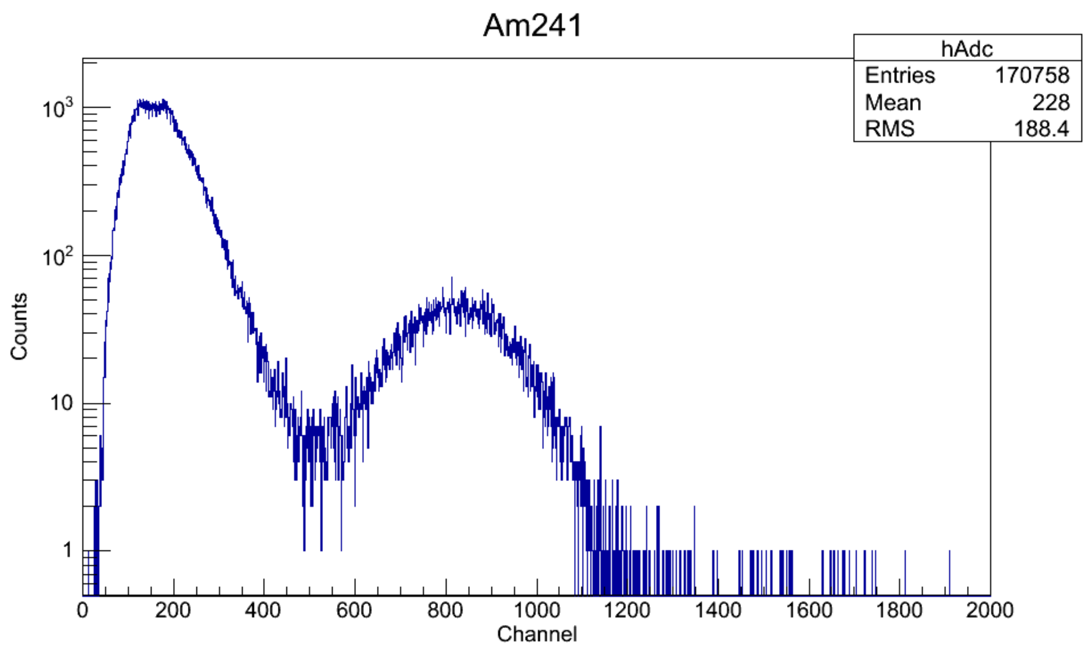

Figure 4.1: ^{241}Am 59 keV calibration with detector operating at -2300 V.

4.2.2 TDC Calibration

A TDC calibrator module was used to calibrate the TDC. Each pulse emitted by calibrator has a known 100 ns separation. The TDC scale is set at 500 ns, with a total of 2000 channels, each channel is about 0.25 ns. A plot of recorded event peaks and their time are shown in Figure 4.2. Using a linear fit, the calibration was determined to be 0.2705 ns/channel for Sept. 2014 run and 0.2775 ns/channel for Feb. 2015 run.

This calibration is still not exact, because of the calibrator resolution limit. The more direct reason is that because the flight path is set to be short (174 cm for low energy runs), the energy calculation becomes sensitive to time-of-flight at such short distance.

Although not very precise in calibration, this step confirms that the TDC module has a linear response to time. It provides a reference frame for applying the more precise calibration method, which is to use the multiple characteristic sulfur resonances in the energy region of interest. By aligning resonance peaks to n-S spectrum, the he final calibration, the precision can be promised. More sulfur calibration results are shown in the following sections.

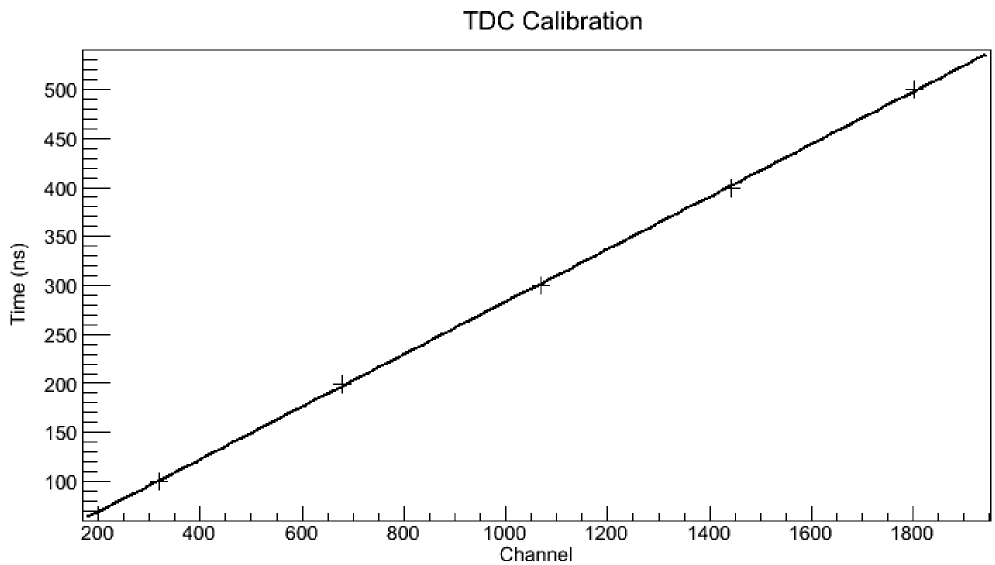

Figure 4.2: TDC calibration using calibrator; x axis is TDC channels; y axis is the time of the calibrator signal.

4.2.3 TDC Time Walk Correction

There are still observable time walks that need to be corrected, even if the constant fraction discrimination(CFD) module has been set carefully. The ADC vs. TDC plot in Figure 4.3 shows a example spectrum of the effect. The green band from (TDC: 1760, ADC: 200) to (TDC: 1770, ADC: 1800) is the region that needs to be corrected. This band represents early arriving γ rays, because γ rays travels at the same speed (speed of light), they should arrive at the same time. So the goal is to correct this band into a vertical band.

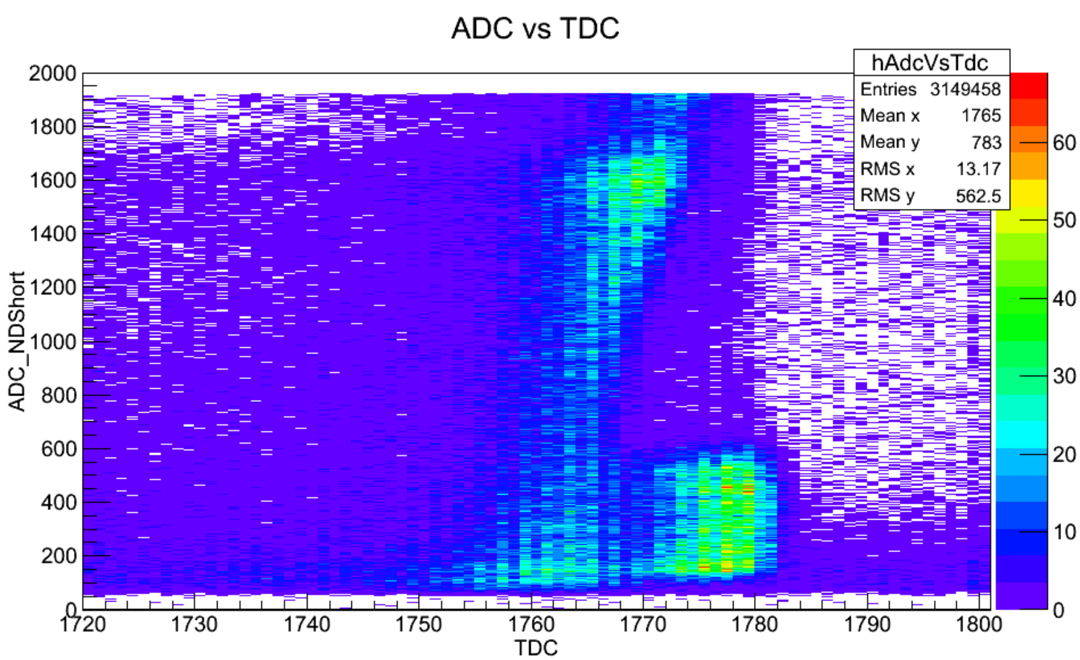

Figure 4.3: ADC vs. TDC on γ flash from run #318.

Since the shape is nearly linear, we can apply a linear fit on the time walk for the γ ray band as a good approximation,

$$TDC_{corrected} = TDC + \frac{TDCShiftedWidth}{ADCMaxHeight} * (ADCMaxHeight - ADC) \quad (4.1)$$

The correction result is shown in Figure 4.4.

Notice there exists another higher-density short band to the right of the γ-ray band in both figures. The reason for this is not yet known. Several separate runs

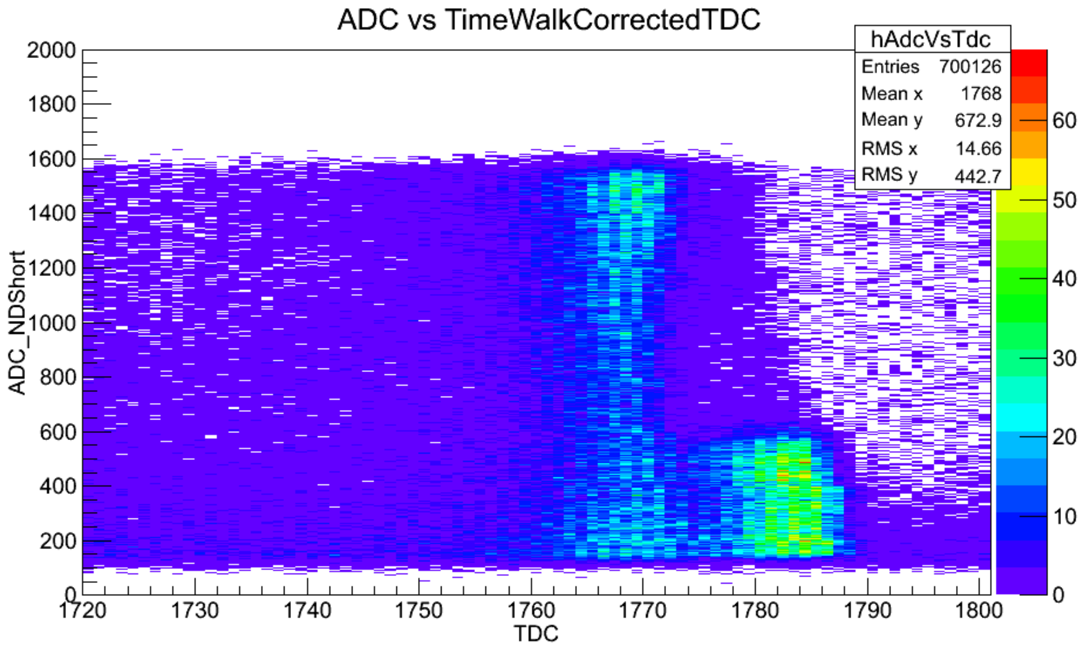

Figure 4.4: ADC vs. TDC on γ flash after time walk correction.

has been dedicated for identifying the source of it, but up to this time, it is still not certain whether it is the problem of the beam line or it is created by reactions other than the ^{7}Li(p, n)^{7}Be reaction. There is no evidence that this extra peak has any interference with respect to the later neutron event. Additionally, from the calibration from multiple n-S resonance peaks, the γ ray band on the left is confirmed to be the γ ray created at the time of neutron creation. This extra peak will be ignored during the following analysis.

4.2.4 n-S spectrum calibration

As mentioned above, the sulfur sample was used for the precise time-of-flight calibration, because it has multiple easy-to-identify resonances below 1 MeV as shown in Figure 4.5

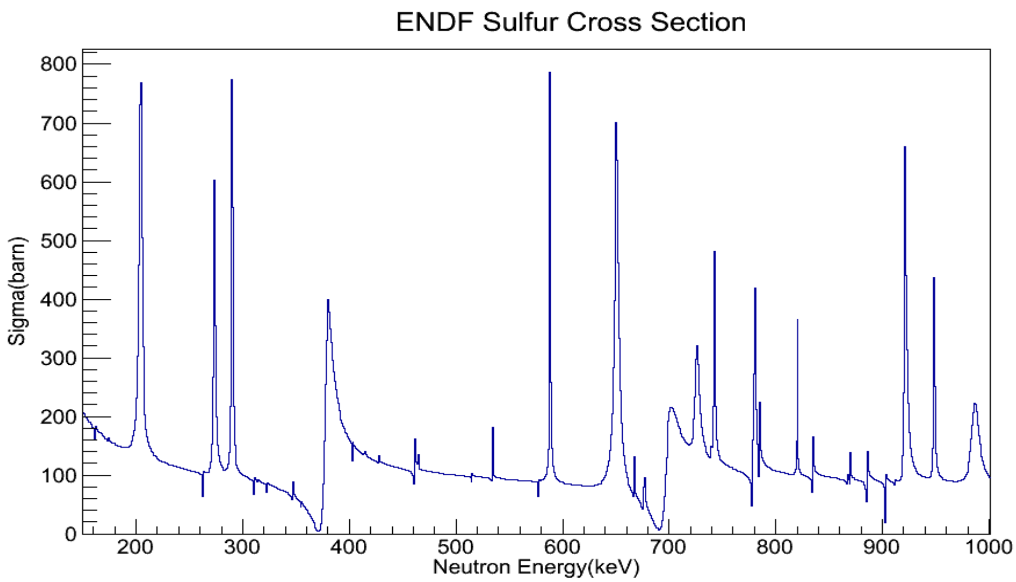

Figure 4.5: Spectrum of n-S resonances from ENDF.

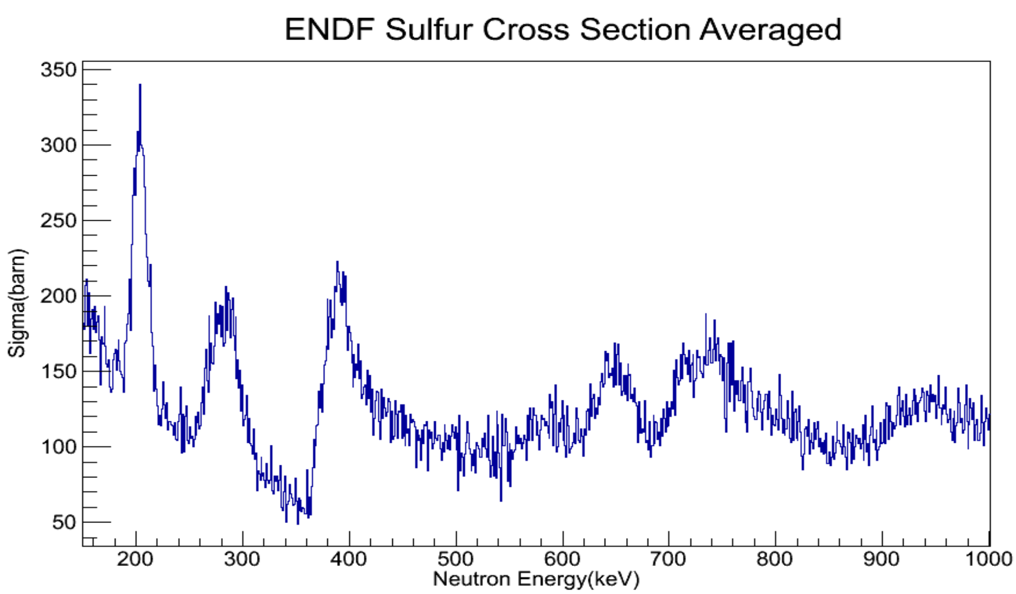

Figure 4.6: Simulated n-S cross sections based on ENDF data.

In order to compare with the real spectrum, a Monte Carlo sampling method was used to simulate the cross section distribution using a factor of 3% random distribution. The simulation result is shown in Figure 4.6

Then, according to the available experiment data we currently have, we can chose two characteristic energies from both the high and low parts of the sulfur resonances, 200 keV and 690 keV, respectively.

Figure 4.7 shows a overall view of our Sept. 2014 data. It shows good agreement with the theoretical spectrum.

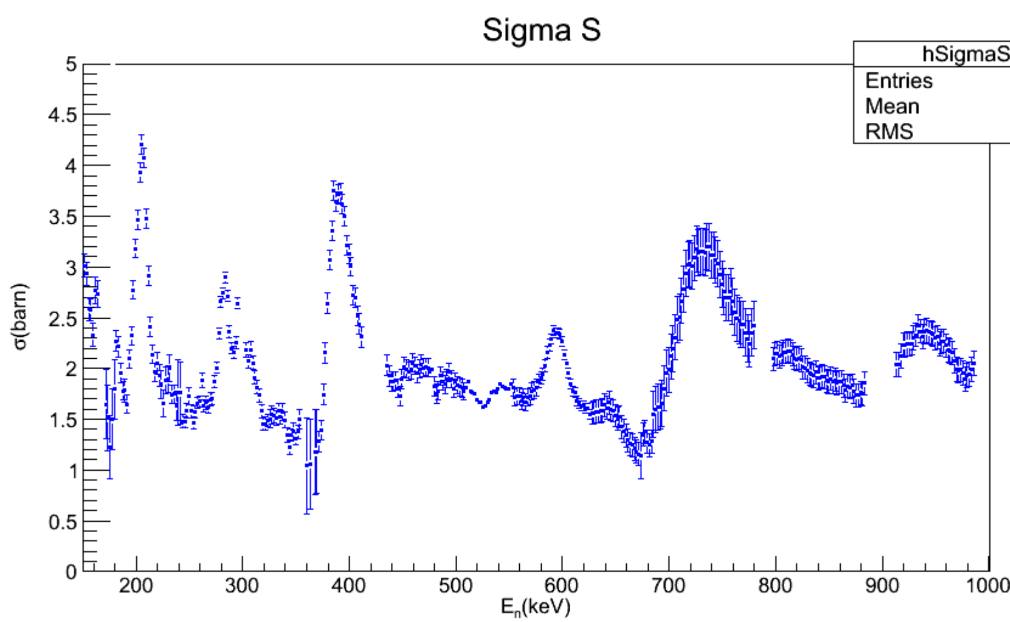

Figure 4.7: Experiment data of n-S cross sections from Sept. 2014.

A more detailed 200 keV resonance comparison between the ENDF data and our results are shown in Figure 4.8 Figure 4.9 and Figure 4.10.

And 690 keV resonance comparison is shown in Figure 4.11 and Figure 4.12.

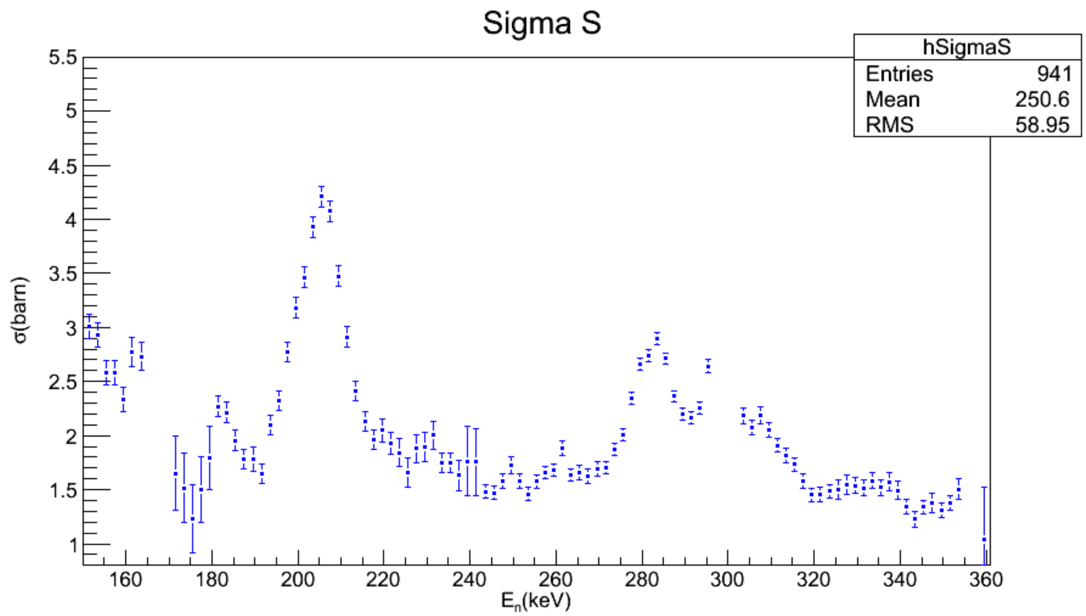

Figure 4.8: Resonance of n-S cross section at 200 keV, Sept. 2014.

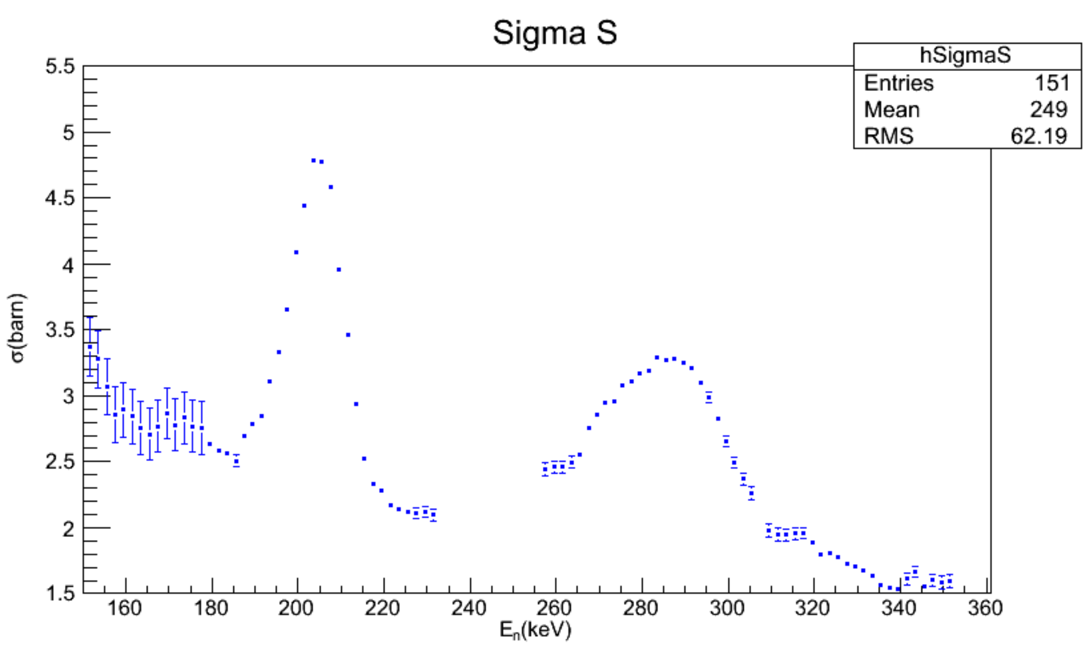

Figure 4.9: Resonance of n-S cross section at 200 keV, Feb. 2015.

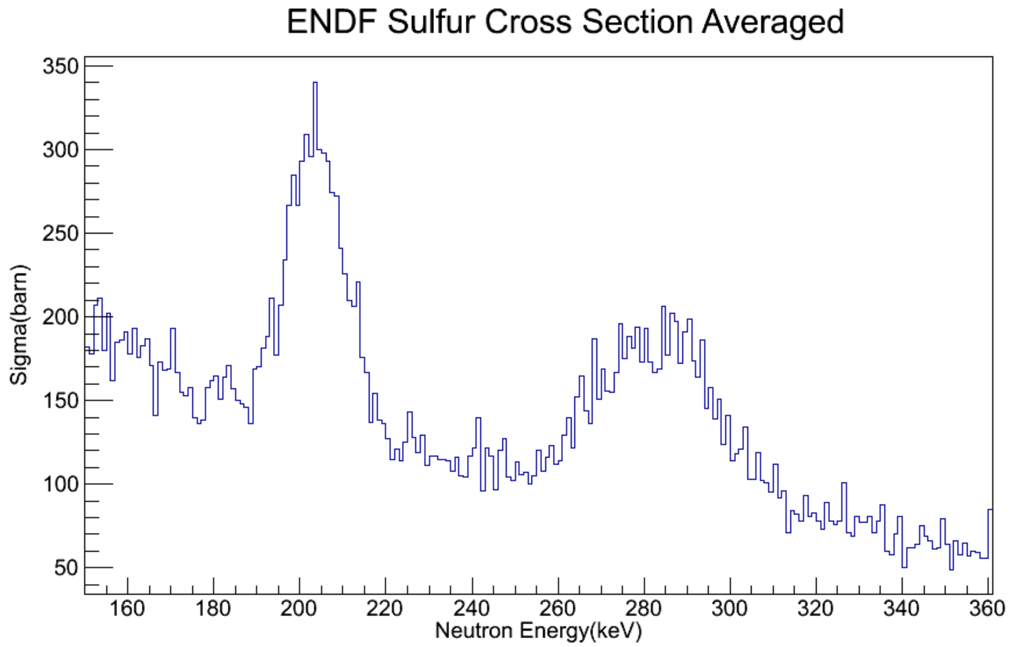

Figure 4.10: Simulated n-S cross section resonance at 200. keV based on ENDF data.

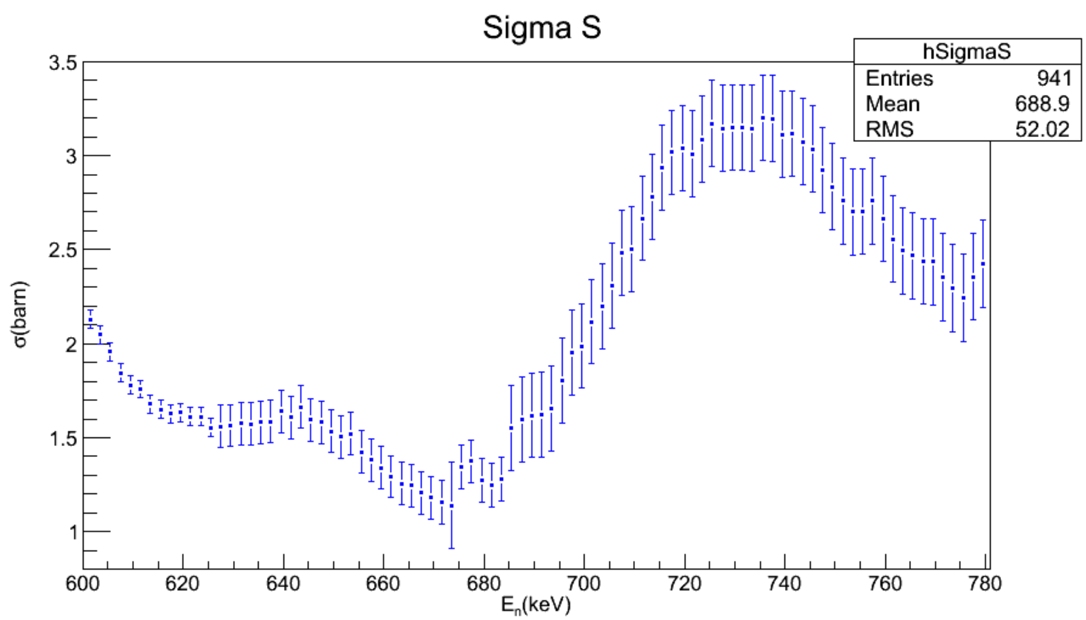

Figure 4.11: Resonance of n-S cross section at 690 keV.

.

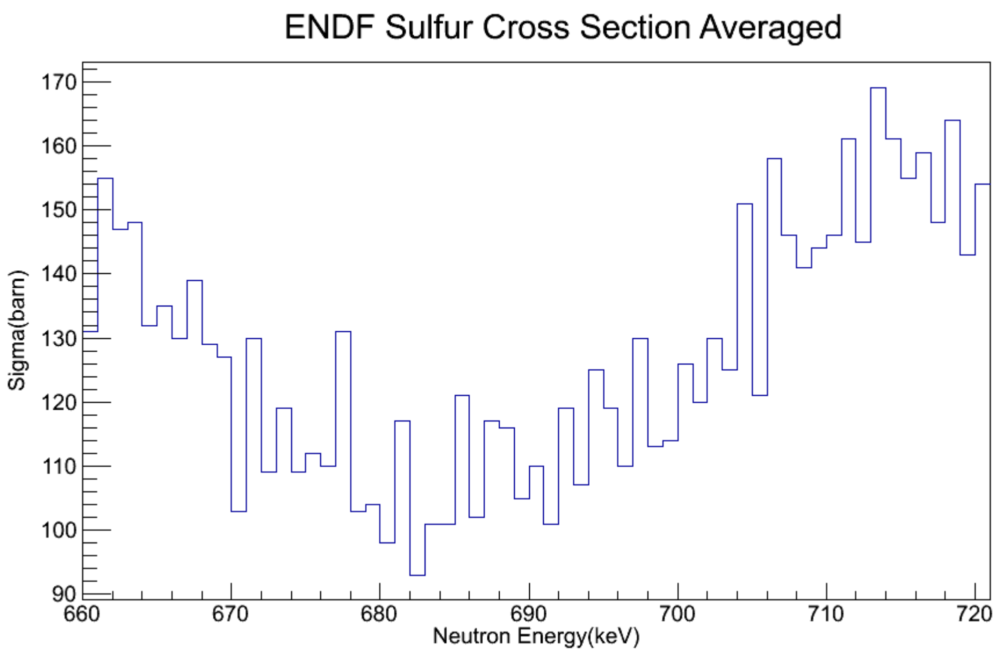

Figure 4.12: Simulated n-S cross section resonance at 690 keV based on ENDF data.

4.3 Cuts

4.3.1 ADC vs TDC

Before setting up any cuts, the first thing to do is to figure out where to find the interesting neutron events. An ADC vs TDC plot shown in Figure 4.13 clearly explains part of it. The horizontal axis of this figure is the TDC spectrum, which is triggered by a detector event and stopped by the next beam pickoff. Since γ rays arrive at the detector earlier than neutron events, the γ events are recorded a longer times to the stop signal, as shown on the right side of the plot. Then looking from right to left, the neutron events coming in with fast neutron events first and following by slower and slower neutron events. So, in order to select only neutron region, they should show up in region with 'right' time and 'right' energy, as shown in Figure 4.14

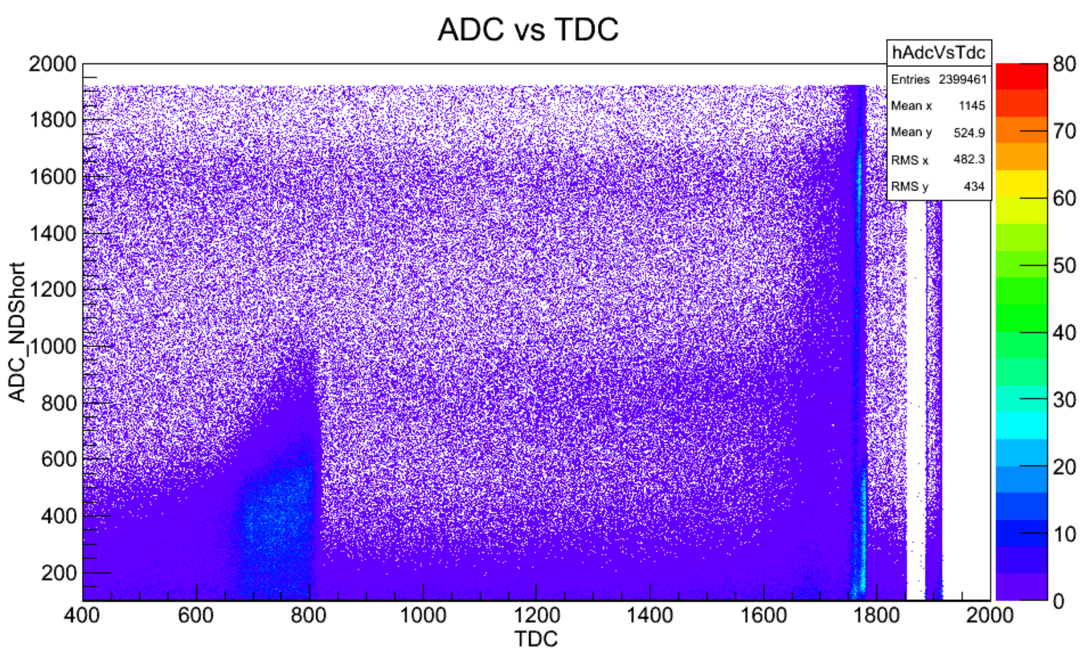

Figure 4.13: ADC vs TDC. ADC is from NDLong signal of raw data, and TDC is chosen from one of the differently delayed signals that can show the whole range of the spectrum.

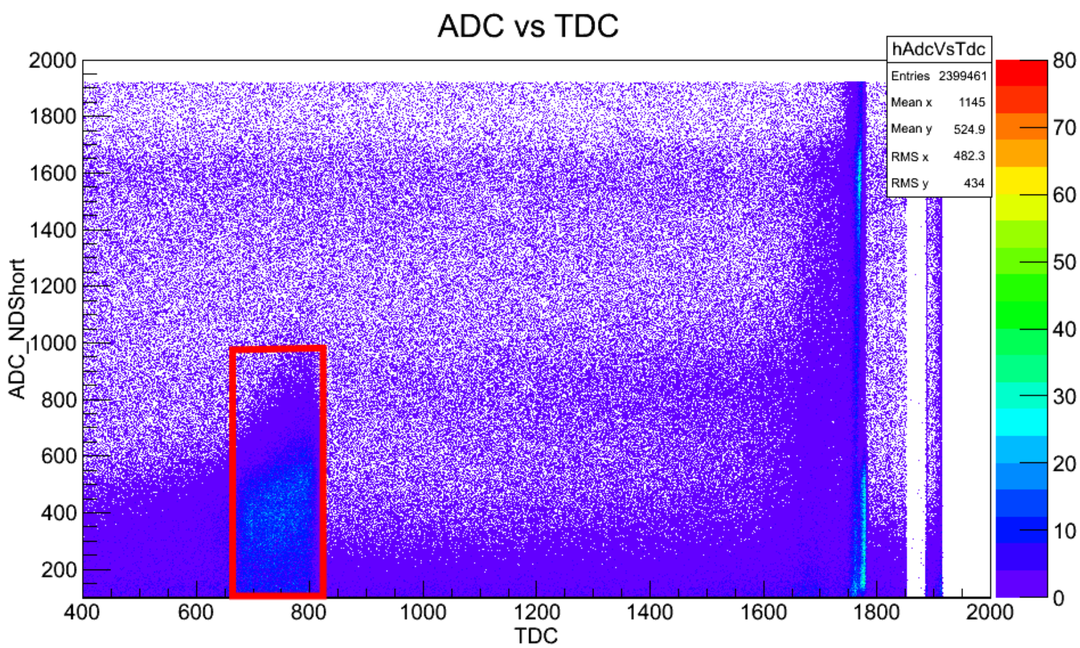

Figure 4.14: ADC cuts and TDC cuts shown as a rectangle in the ADC vs TDC plot.

4.3.2 ADC Cuts

After we applied the cuts from Figure 4.14 shown above, the ADC spectrum can be plotted again, shown in Figure 4.15. Now it is cleaner than what was shown before in Figure 3.1.

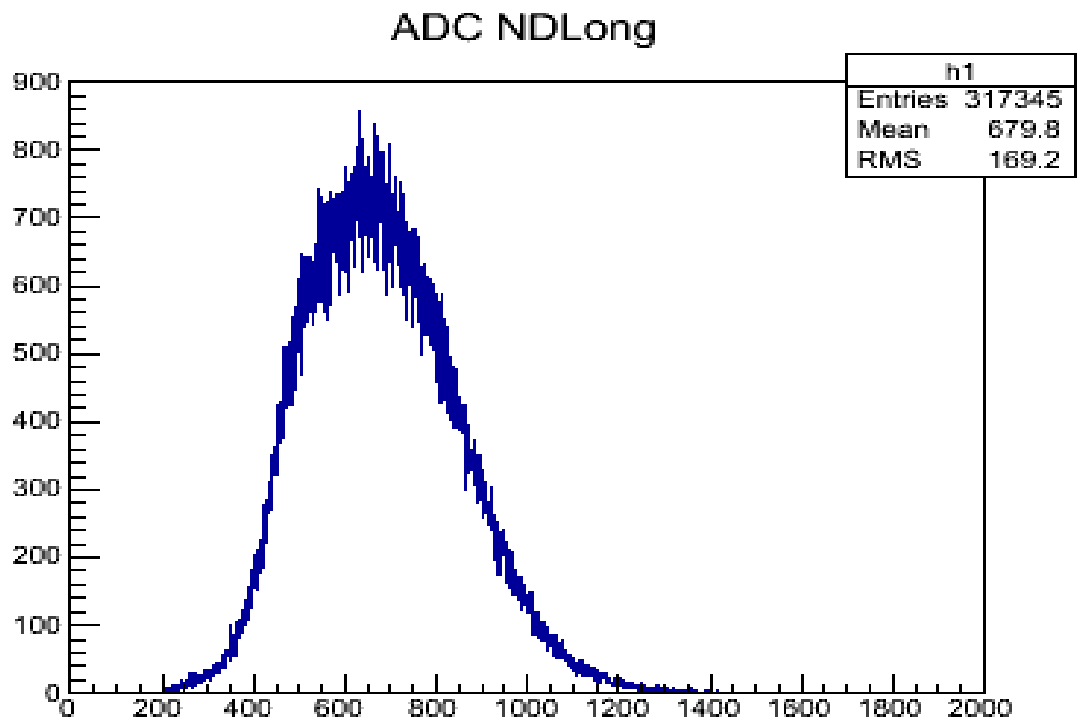

Figure 4.15: An example ADC spectrum after ADC and TDC cuts.

4.3.3 TDC Cuts

Similar to ADC cuts, the TDC spectrum can also be plotted with cuts applied, as shown in Figure 4.16, which shows all TDC data of a whole single run. To separate out data from each sample, the sample ID spectrum can be used to set the new cut on sample selection. As an example, the 2 cm CH_2 and one Blank sample were plotted in Figure 4.17 and Figure 4.18.

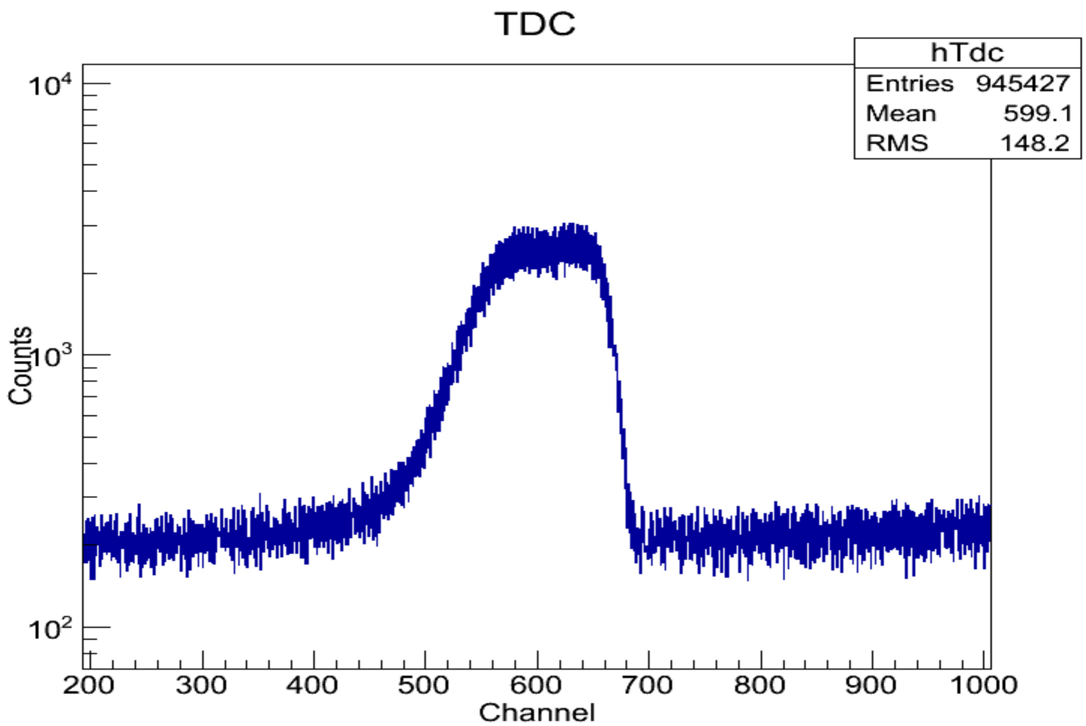

Figure 4.16: An example TDC spectrum after ADC and TDC cuts.

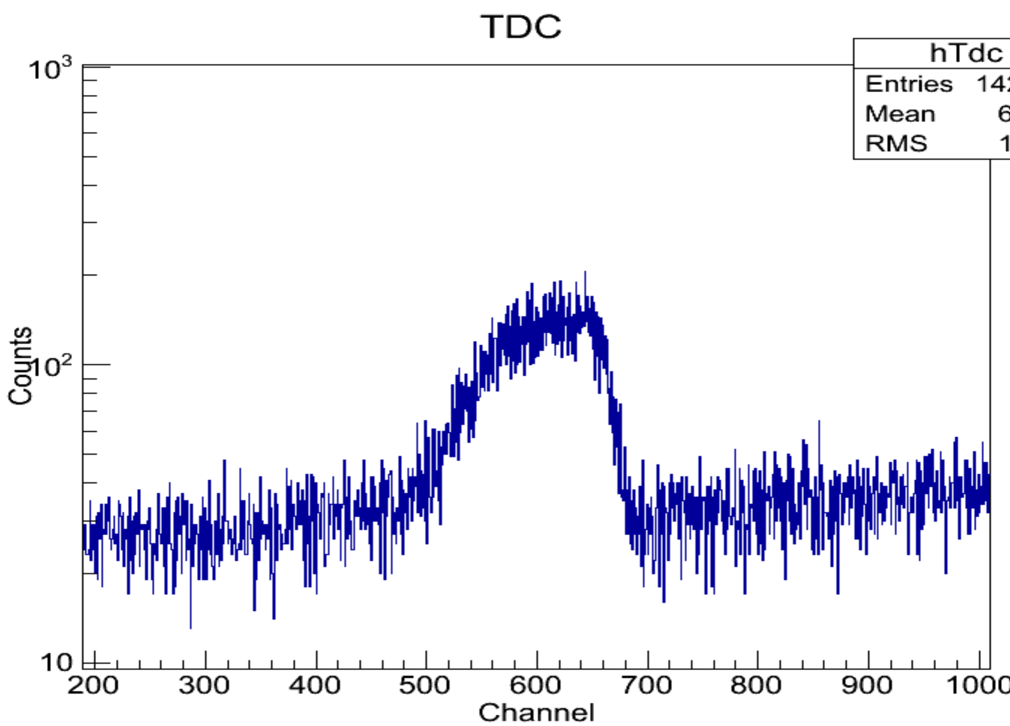

Figure 4.17: An example TDC spectrum of 2 cm CH_2 after ADC and TDC cuts were applied.

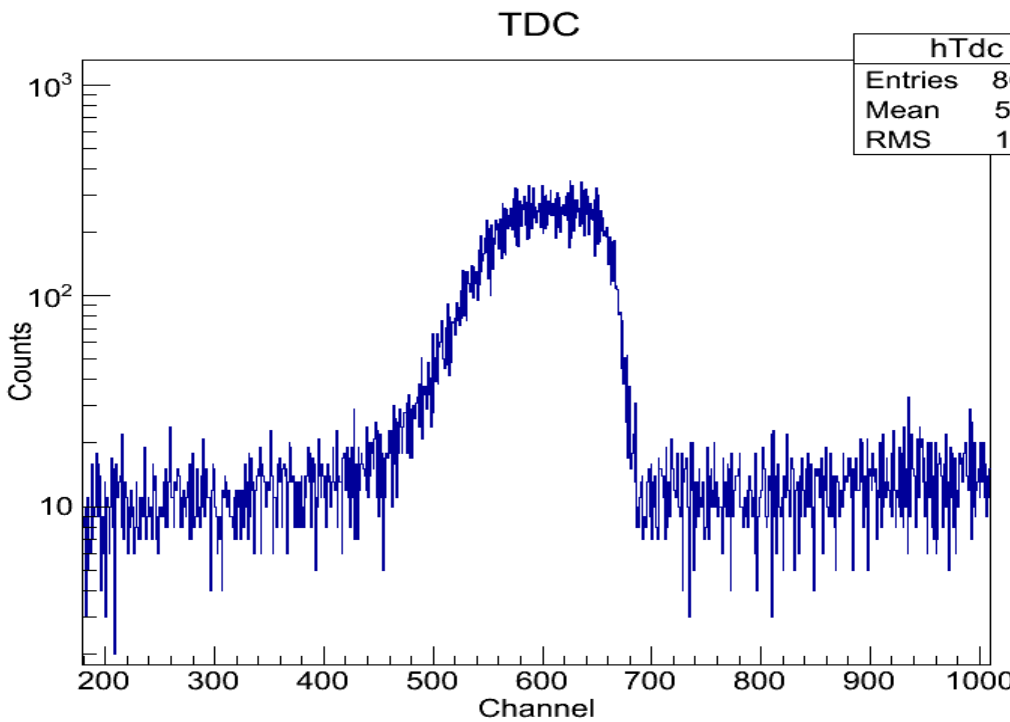

Figure 4.18: An example TDC spectrum of the Blank sample after ADC and TDC cuts were applied.

4.3.4 PSD Cuts

Besides energy and time considerations, the events left now consist of both neutrons and γ-rays. To distinguish them, the 'pulse shape discrimination(PSD)' method is used, which is based on the fact that scintillators respond differently to protons and electrons.

For a given total energy γ rays are generally sharper than neutron events, or neutron events generally have longer tails than γ ray events. By integrating the pulse energy partially and comparing with its total energy, their characteristics can be plotted on a 2-D graph, as shown in Figure 4.19. In the plot, the vertical axis is the long-gated ADC, or total pulse energy deposited in the detector. The horizontal axis is the short-gated ADC reading; the gate is set to only allow the head of the pulse been integrated, typically 30 - 80 ns wide depending on the incident neutron energy. So, for pulses with the same total energy, neutron events should have smaller head in comparison with γ rays, which is represented by the lower left band shown in the plot. And γ rays are shown in the upper right band. There are some modifications on the horizontal axis calculation which are intended to amplify the difference; the exact calculation is

$$x = \frac{\text{NDShort}}{\text{NDLong} + a} * b, \tag{4.2}$$

where by tunning the values of a and b, depending on the gate settings for a specific run, a combination can then be found so that the two bands can have a clearer separation. For low-energy runs, the typical values were chosen to be $a = 100$ and $b = 1800$.

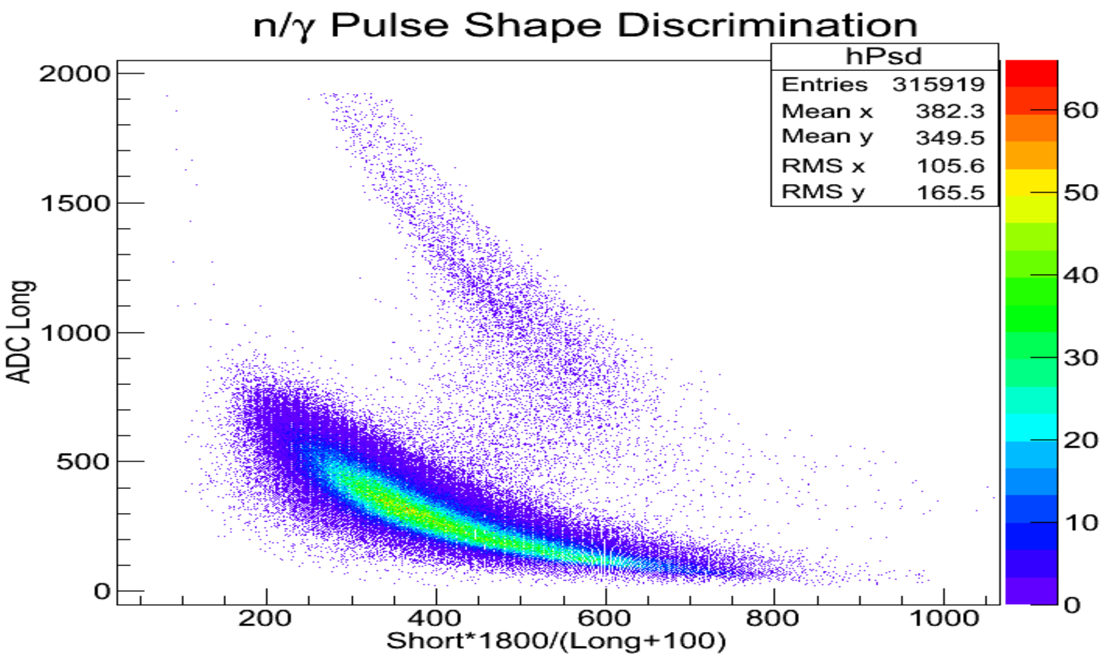

Figure 4.19: Pulse-shape discrimination; y axis is ADC from NDLong signal; x axis is calculated(4.2) result based on ADC NDShort signal.

4.4 Background Subtraction

Background signals exist all the time during data collection, because they are random events. The TDC spectrum clearly shows their distribution, which can be described as expected by a linear line

$$y = ax + b, \tag{4.3}$$

where x represents the TDC channel and y is number of counts. Coefficients a and b can be calculated by

$$a = \frac{n\Sigma_{i=1}^{n} x_i y_i - (\Sigma_{i=1}^{n} x_i)(\Sigma_{i=1}^{n} y_i)}{n\Sigma_{i=1}^{n} x_i^2 - (\Sigma_{i=1}^{n} x_i)^2} = \frac{SS_{xy}}{SS_{xx}} \tag{4.4}$$

$$b = \frac{(\Sigma_{i=1}^{n} x_i)^2(\Sigma_{i=1}^{n} y_i) - (\Sigma_{i=1}^{n} x_i y_i)(\Sigma_{i=1}^{n} x_i)}{n\Sigma_{i=1}^{n} x_i^2 - (\Sigma_{i=1}^{n} x_i)^2} = \bar{y} - a\bar{x}, \tag{4.5}$$

where their uncertainties are

$$\delta_a = \sqrt{\frac{s_{y,x}^2}{SS_{xx}}} \tag{4.6}$$

$$\delta_b = \sqrt{\frac{s_{y,x}^2 \Sigma_{i=1}^{n} x_i^2}{nSS_{xx}}} = \sqrt{s_{y,x}^2 (\frac{1}{n} + \frac{\bar{x}^2}{SS_{xx}})}, \tag{4.7}$$

where

$$\begin{aligned} s_{y,x}^2 &= \frac{\Sigma_{i=1}^{n}(y_i - (ax_i + b))^2}{n-2} \\ &= \frac{\Sigma_{i=1}^{n} y_i^2 - 2a\Sigma_{i=1}^{n} x_i y_i - 2b\Sigma_{i=1}^{n} y_i + a^2\Sigma_{i=1}^{n} x_i^2 + 2ab\Sigma_{i=1}^{n} x_i + b^2 n}{n-2} \end{aligned} \tag{4.8}$$

$$SS_{xx} = \Sigma_{i=1}^{n}(x_i - \bar{x})^2. \tag{4.9}$$

And finally, after considering background,

$$Y_{\text{neutron}} = Y_{\text{raw}} - Y_{\text{background}}, \tag{4.10}$$

with

$$\delta Y_{\text{neutron}} = \sqrt{\delta_{Y_{\text{raw}}}^2 + \delta_{Y_{\text{background}}}^2}. \tag{4.11}$$

Figure 4.20 shows an example of how we apply the background fit. Notice that on the left side of this plot, the fitting line cannot describe all the backgrounds we observe. That introduces our next step in background subtraction.

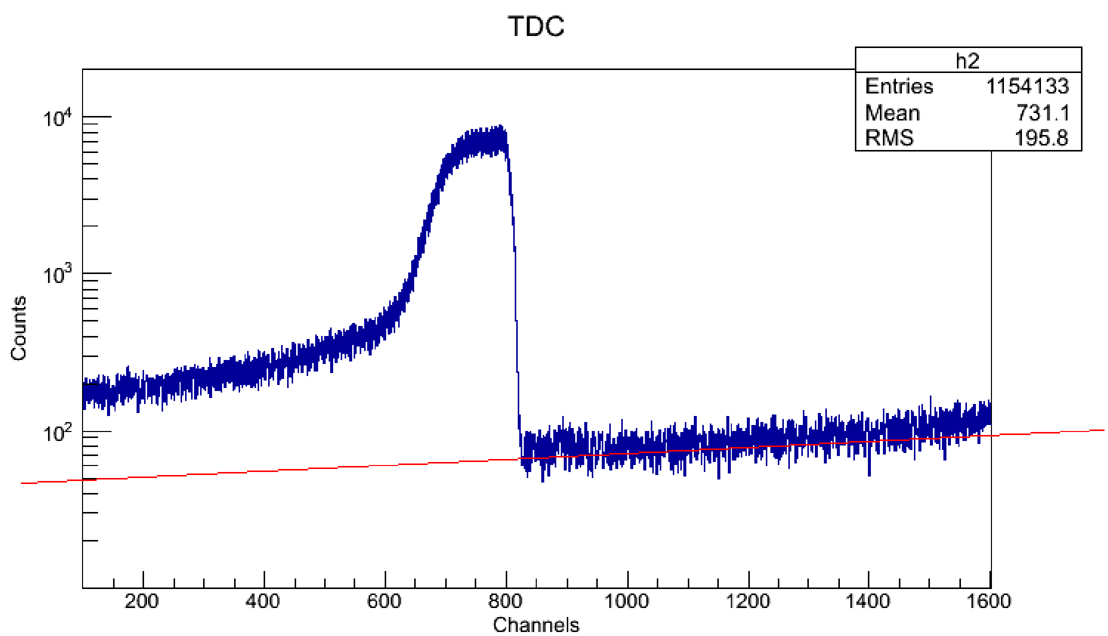

Figure 4.20: An example background fit on a TDC spectrum.

4.5 Dead Time and Normalization

In order to calculate cross sections, both sample in and sample out yields are needed. More specifically, the yields should be under the same condition; except only the sample has been put in and out. This introduces the consideration of beam intensity and electronics dead time.

With these corrections, the 'net yield' can be defined as

$$Y = Y_{\text{neutron}} \cdot f_{\text{dead time}} \cdot f_{\text{norm}}, \tag{4.12}$$

with

$$\delta_Y = Y \cdot \sqrt{\left(\frac{\delta_{Y_{\text{neutron}}}}{Y_{\text{neutron}}}\right)^2 + \left(\frac{\delta_{f_{\text{dead time}}}}{f_{\text{dead time}}}\right)^2 + \left(\frac{\delta_{f_{\text{norm}}}}{f_{\text{norm}}}\right)^2}. \tag{4.13}$$

4.5.1 Dead-Time Correction

The dead-time is the time needed by the electronics to collect one event before it's ready to collect the new one. It has a dependency on the event rate, and is usually several microseconds per event. In this experiment, the count rate is around several hundred per second, the dead-time is about $< 5\%$.

Figure 4.21 shows some typical values of dead-time correction for a single run.

Notice that the data from the neutron detector is far above the other two results. This is because the CFD module is generating multiple triggers for one event. Although it won't affect other data because the veto signal from FERA will block the following triggers, it did mean that the dead-time correction cannot be done by counting raw triggers and accepted triggers. Since the values calculated from the charge integrator and the long counter agree with each other well, and both of them indicate a resonable number ($< 2\%$, which is what we should expect from FERA characteristics), the average of their values were used to do the corrections.

4.5.2 Normalization

Because the beam intensity has variations over time, to make all the yields comparable, a normalization is needed. A good way to do it is to normalize the yields to the beam intensity.

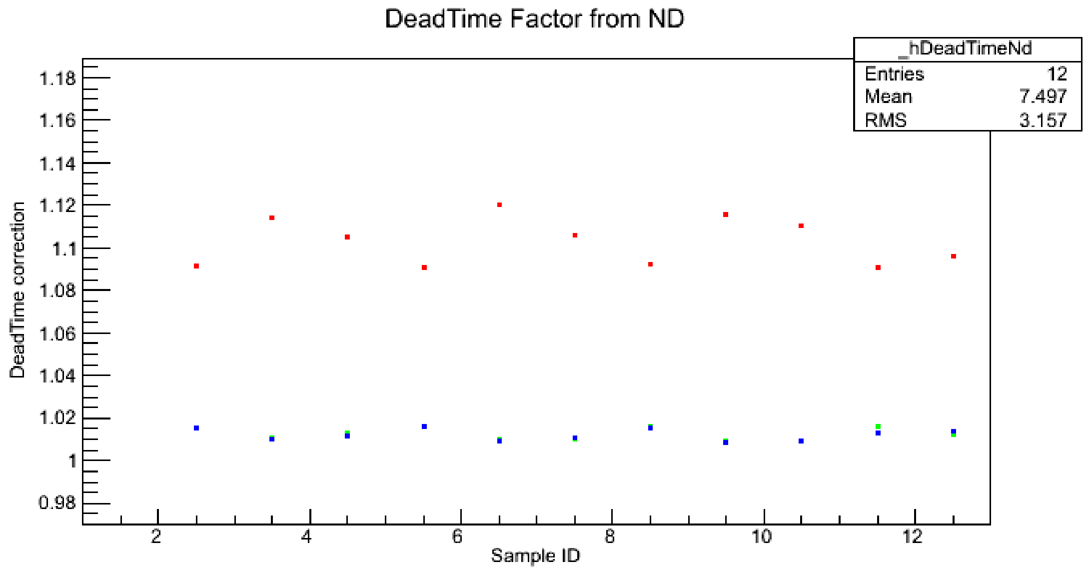

Figure 4.21: Dead-time correction factors for one run. Red dots are calculated from neutron detector triggers, green and blue dots (mostly overlapped) are calculated from the charge integrator and the long counter counts, respectively.

Figure 4.22 shows one example of normalization factors for all samples. Again, both the charge integrator and the long counter give similar results, which means both of them are reliable beam intensity monitors. Because of the dwelling times on each sample are not the same, they have large variations and their normalization factors are very different. Except all the blank samples should be the same, which can be confirmed in the plot.

To further compare the difference of two methods of normalization, the ratios of the two were plotted in Figure 4.23 and Figure 4.24 with different scales.

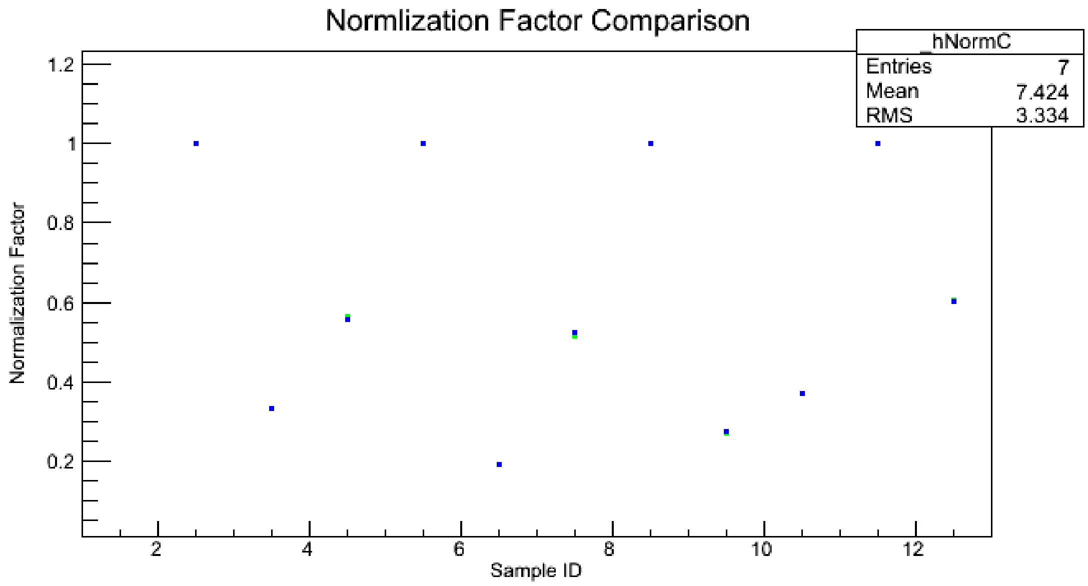

Figure 4.22: Normalization factors from one run, blue and green dots(mostly overlap) are calculated from charge integrator and long counter, respectively.

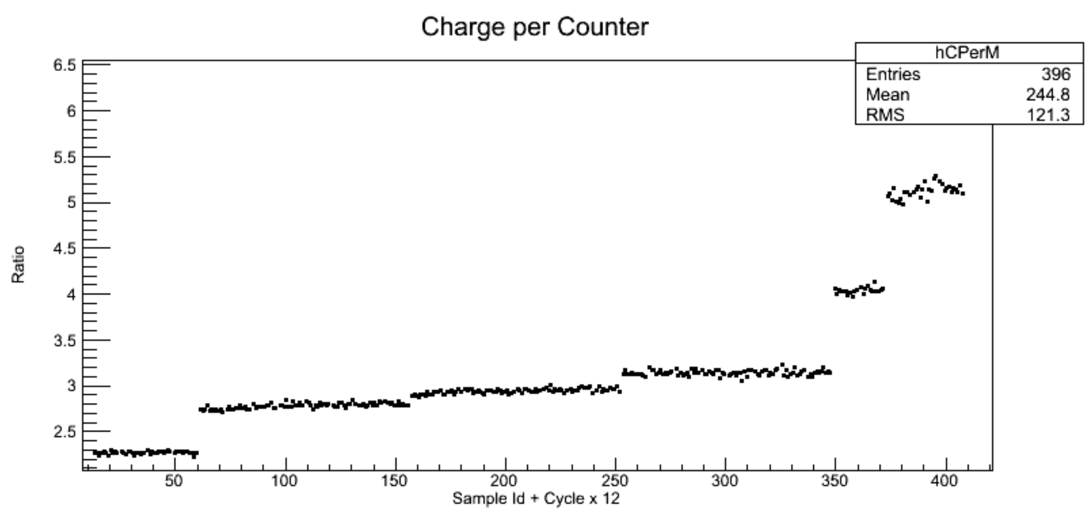

Figure 4.23: Average charge integrator reading per long counter count overview of all runs.

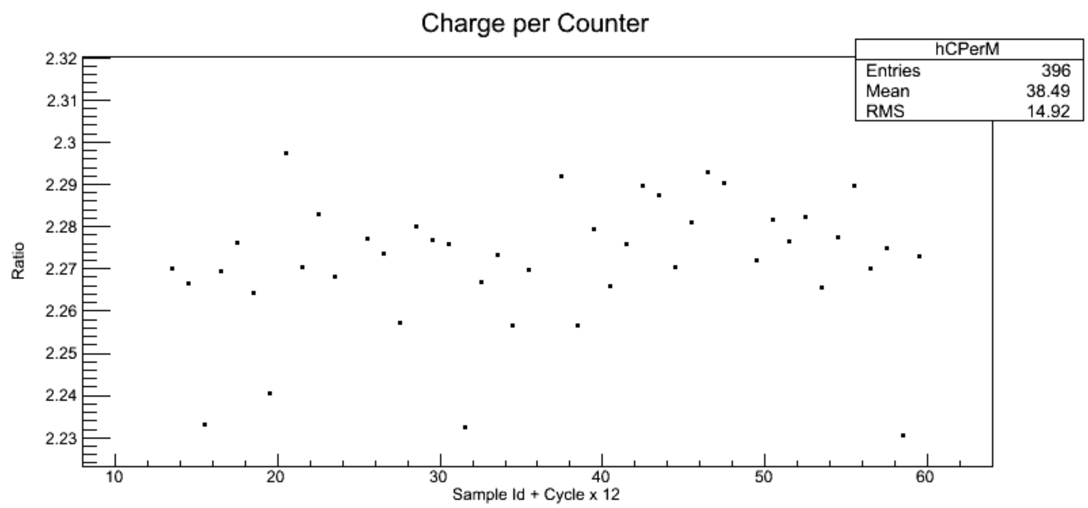

Figure 4.24: Average charge integrator reading per long counter count in a few consecutive runs.

4.6 Results

Finally, with the 'net yields' available, the cross sections can be calculated using the equations mentioned in Section 2.1.

$$\sigma = \frac{\alpha}{\tau} \cdot \ln \frac{Y_{\text{Out}}}{Y_{\text{in}}}, \tag{4.14}$$

with

$$\delta_\sigma = \frac{\alpha}{\tau} \cdot \sqrt{\left(\frac{\delta_{Y_{\text{out}}}}{Y_{\text{out}}}\right)^2 + \left(\frac{\delta_{Y_{\text{in}}}}{Y_{\text{in}}}\right)^2 + \left(\ln \frac{Y_{\text{Out}}}{Y_{\text{in}}} \cdot \frac{\delta_\tau}{\tau}\right)^2}, \tag{4.15}$$

where

$$\alpha = \frac{A}{N_A \cdot \rho}. \tag{4.16}$$

Figure 4.25 and Figure 4.26 shows the calculated carbon and CH_2 cross sections for all three thicknesses, respectively, using 10 keV as an energy bin width.

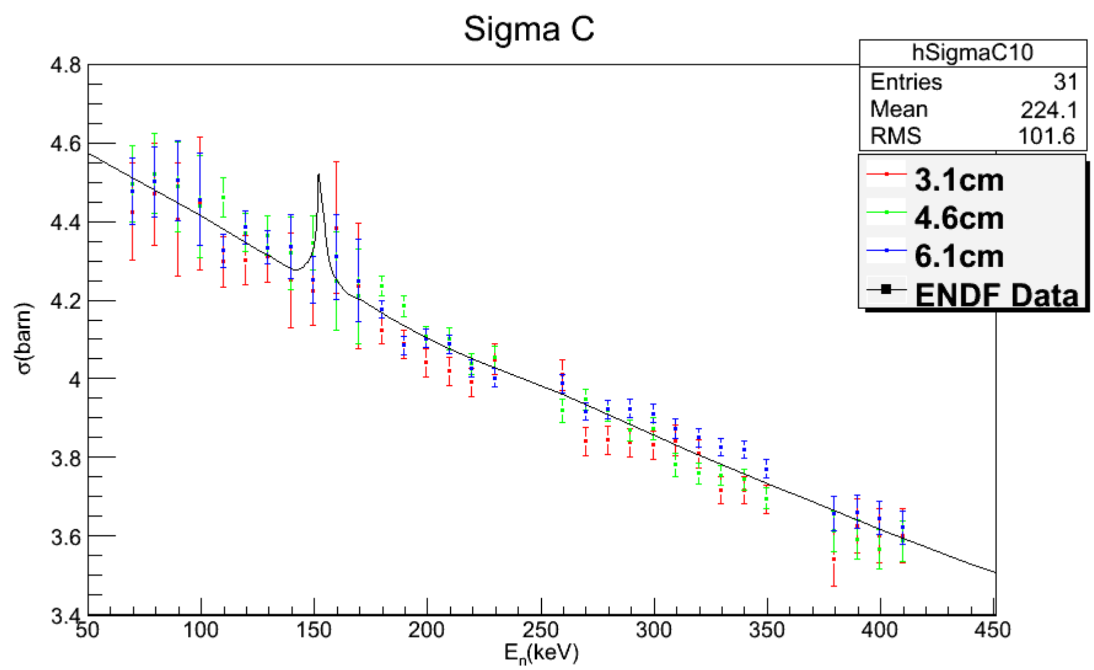

Figure 4.25: n-C cross sections (σ_C) calculated separately from all three sample thicknesses.

The results from different thicknesses are in good agreement with each other. The standard deviations of these different thicknesses are given in Figure 4.27 and Figure 4.28. Figure 4.29 and Figure 4.30 are from Sept. 2014 runs, where the variations

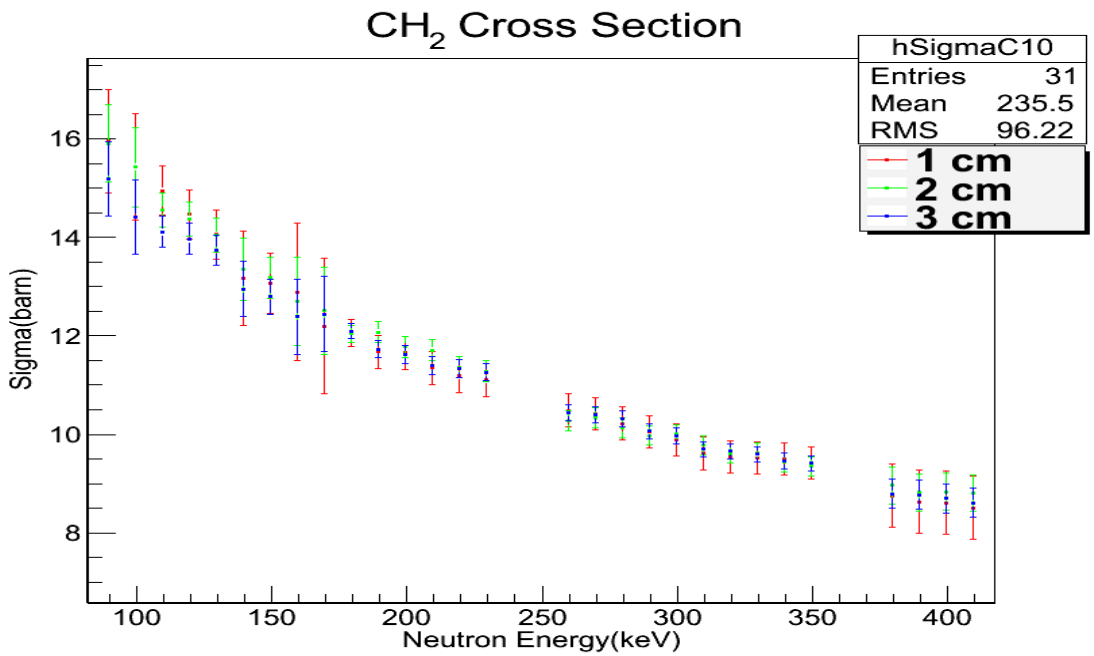

Figure 4.26: $\sigma_{\mathrm{CH_2}}$ calculated separately from all three sample thicknesses.

are bigger at low energies. This is the reason we take the Feb. 2015 run to improve precision.

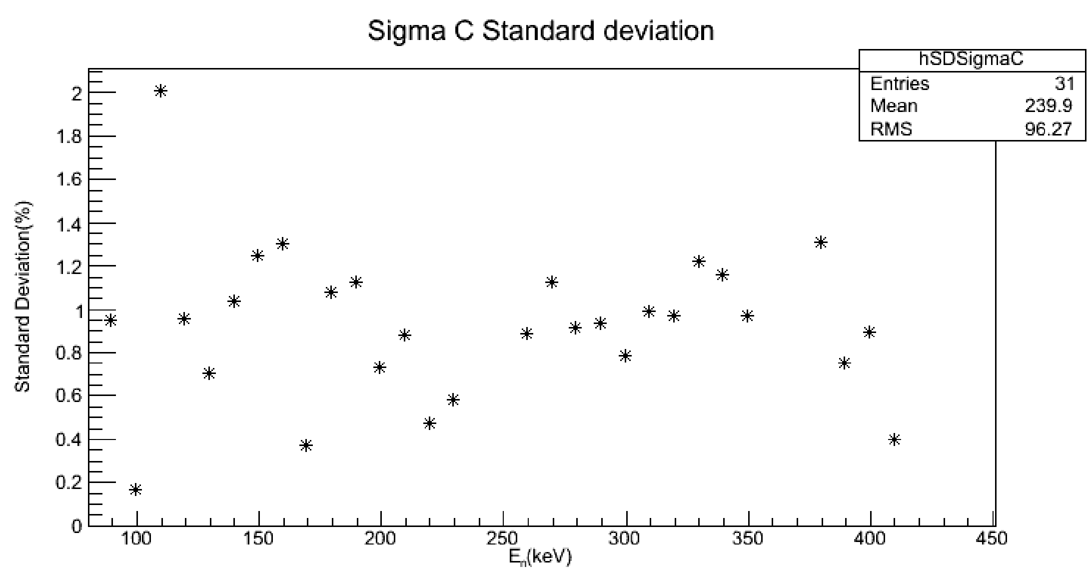

Figure 4.27: The n-C cross section standard deviation ($\delta_{\sigma_{\mathrm{C}}}$) of all three sample thicknesses, Feb. 2015 run.

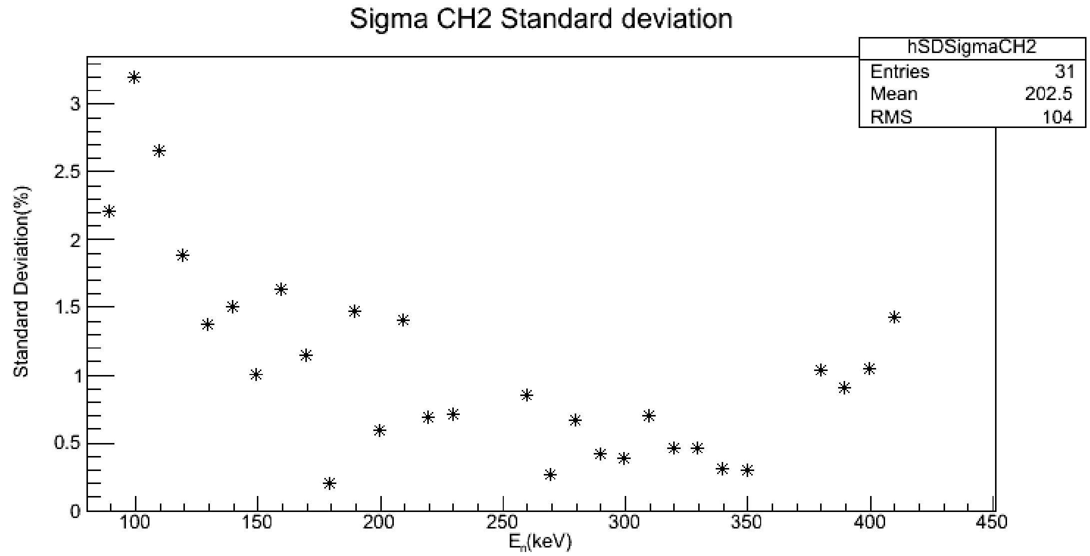

Figure 4.28: The n-CH_2 cross section standard deviation ($\delta_{\sigma_{\mathrm{CH_2}}}$) of all three sample thicknesses, Feb. 2015 run.

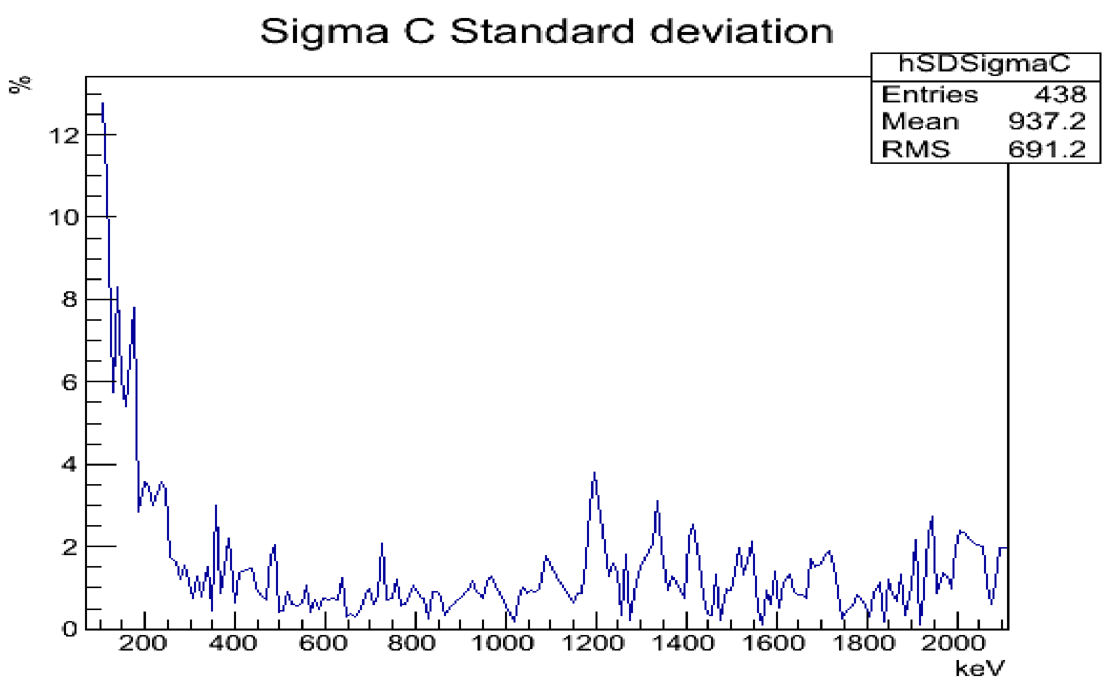

Figure 4.29: The n-C cross section standard deviation ($\delta_{\sigma_{\mathrm{C}}}$) of all three sample thicknesses, Sept. 2014 run.

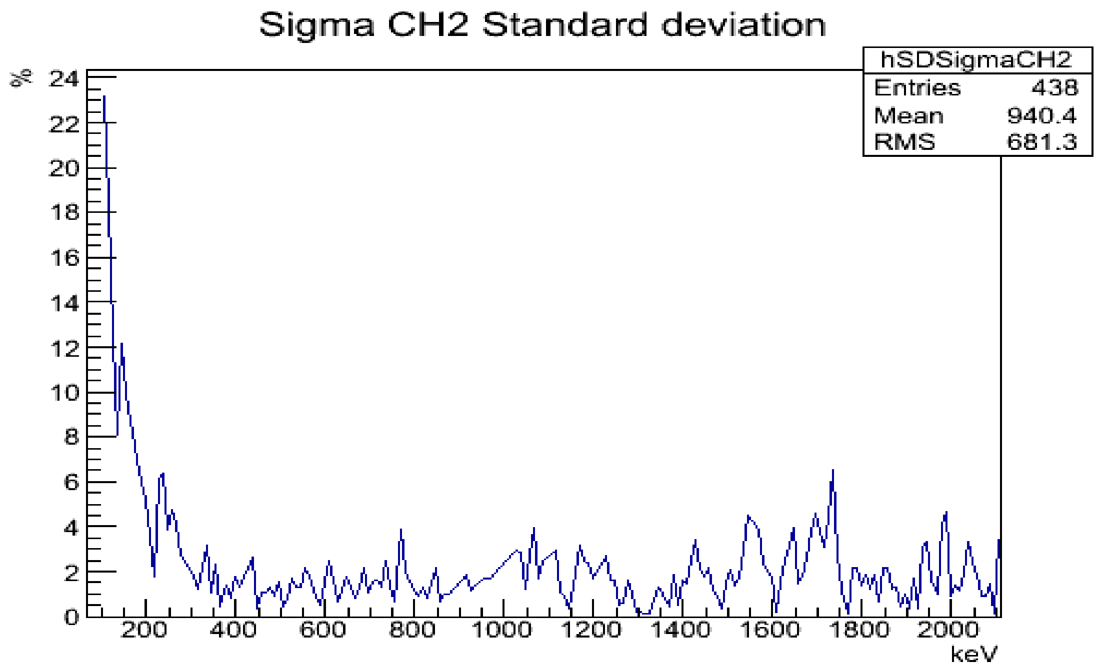

Figure 4.30: The n-CH_2 cross section standard deviation ($\delta_{\sigma_{\mathrm{CH}_2}}$) of all three sample thicknesses, Sept. 2014 run.

Since each single result is an average value from multiple runs, their standard deviation are shown here in Figure 4.31 and Figure 4.32

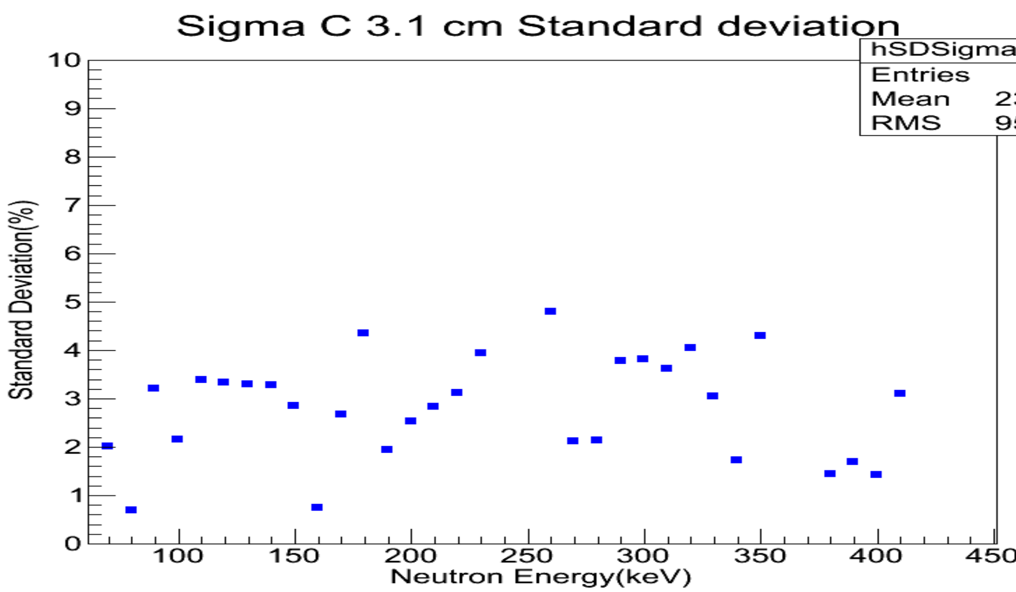

Figure 4.31: The standard deviation (δ_{σ_C}) of the 3.1 cm carbon cross section in all runs from Feb. 2015.

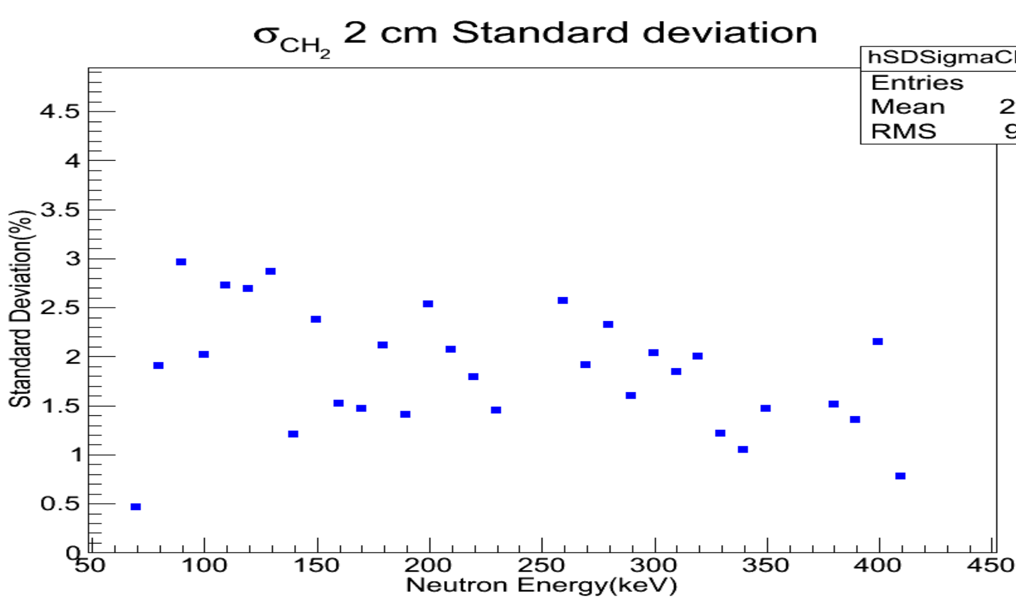

Figure 4.32: The standard deviation ($\delta_{\sigma_{CH_2}}$) of the 2 cm CH_2 cross section in all runs from Feb. 2015.

By doing a weighted average of all thicknesses, the final cross section data can be calculated as shown below in Figure 4.33 and Figure 4.34,

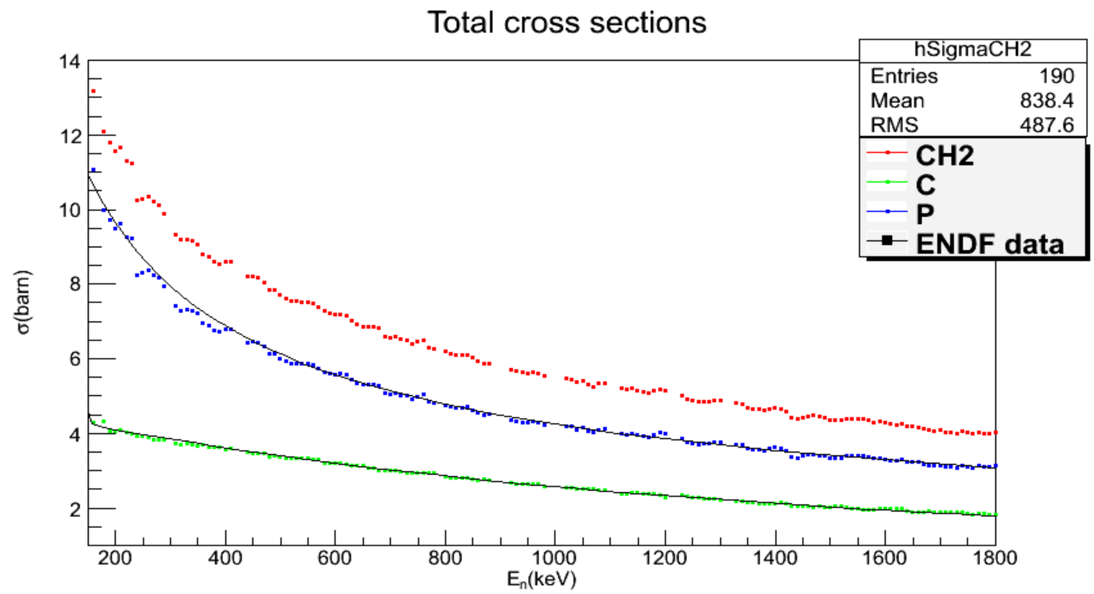

Figure 4.33: The final result of n-p, n-C and n-CH_2 scattering cross sections from the Sept. 2014 run.

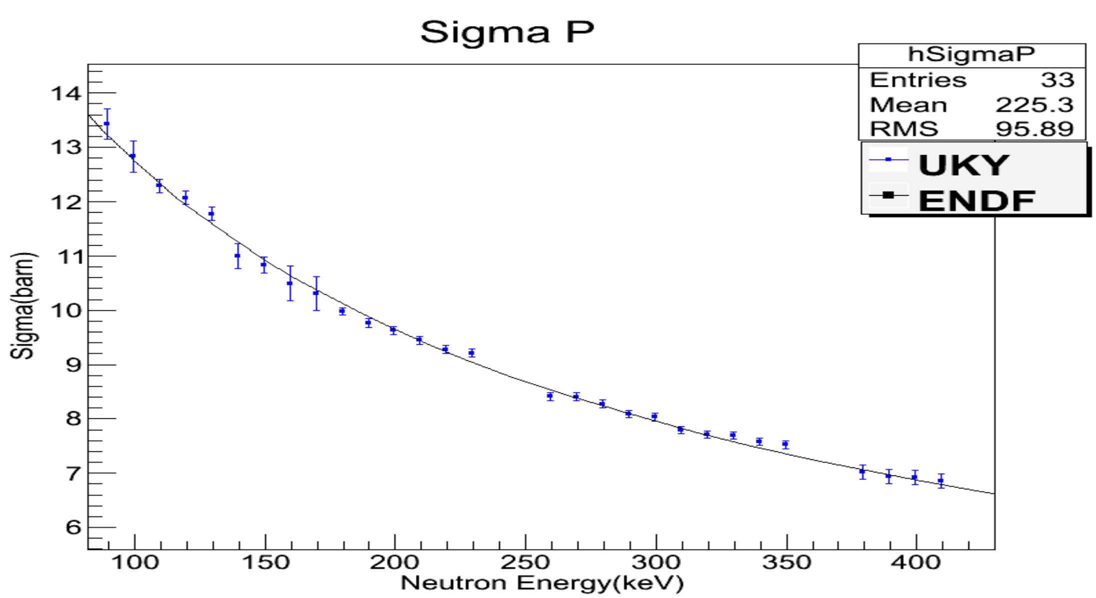

Figure 4.34: The final result of n-p scattering cross sections from the Feb. 2015 run.

A comparision with ENDF data are plotted shown in Figure 4.35, Figure 4.36, Figure 4.37 and Figure 4.38, where the vertical axis is the difference in percentage.

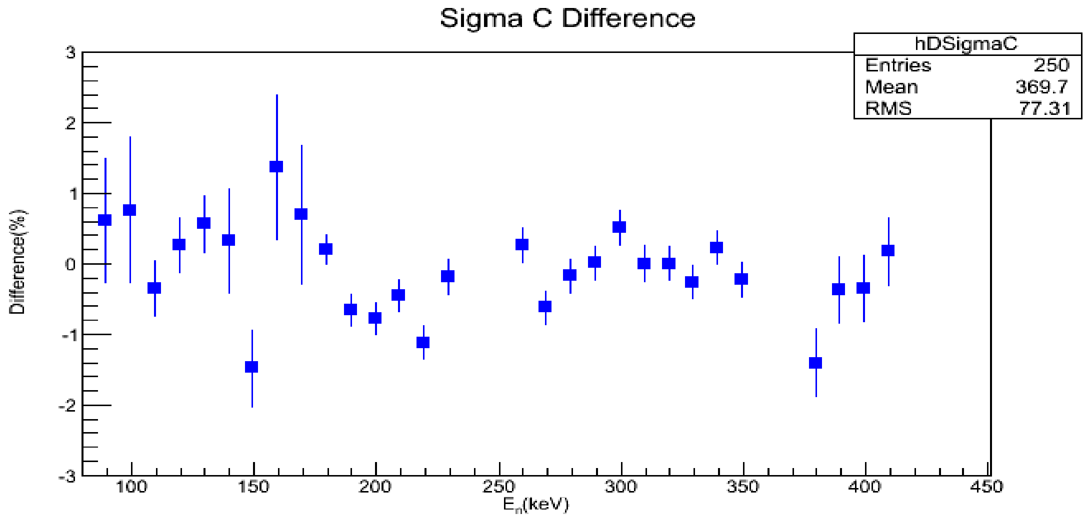

Figure 4.35: Final n-C cross sections (σ_C) in comparison to ENDF tabulated data in the lower-energy region; data are from the Feb. 2015 run.

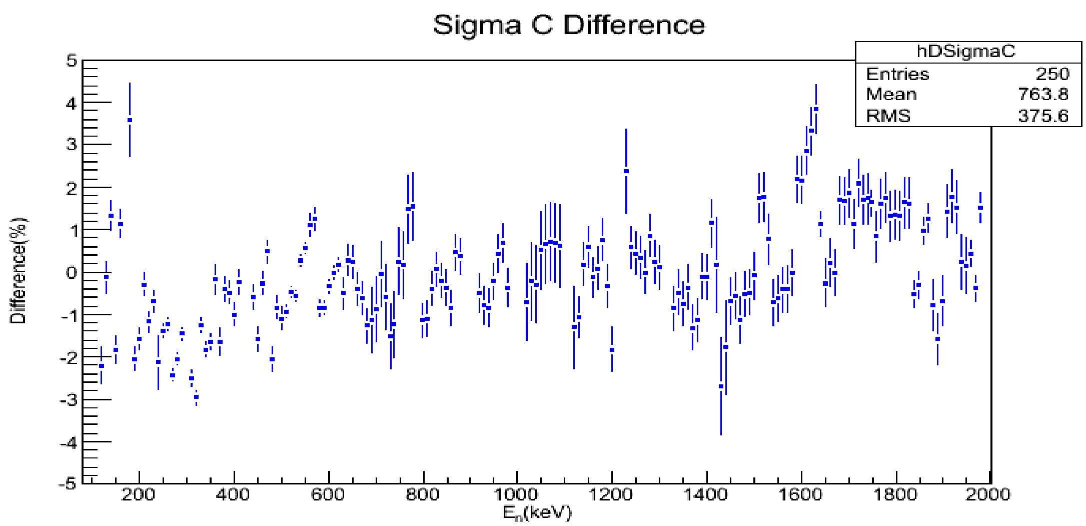

Figure 4.36: Final n-C cross sections (σ_C) in comparison to ENDF tabulated data in the higher-energy region; data are from the Sept. 2014 run.

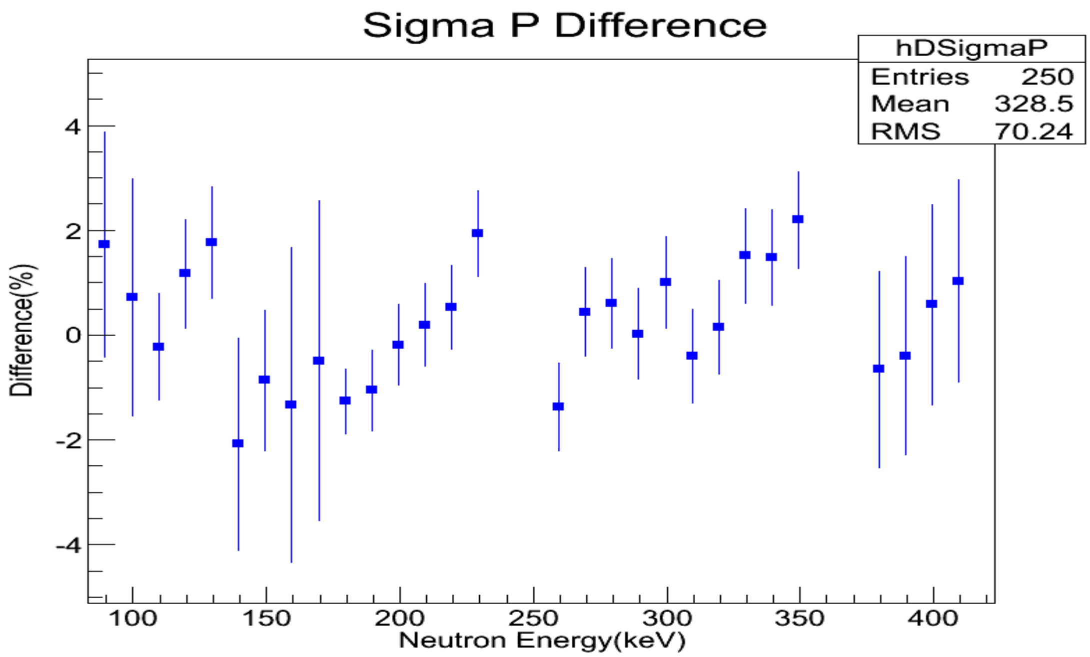

Figure 4.37: The final n-p cross section (σ_p) in comparison to ENDF tabulated data int the lower-energy region; data are from the Feb. 2015 run.

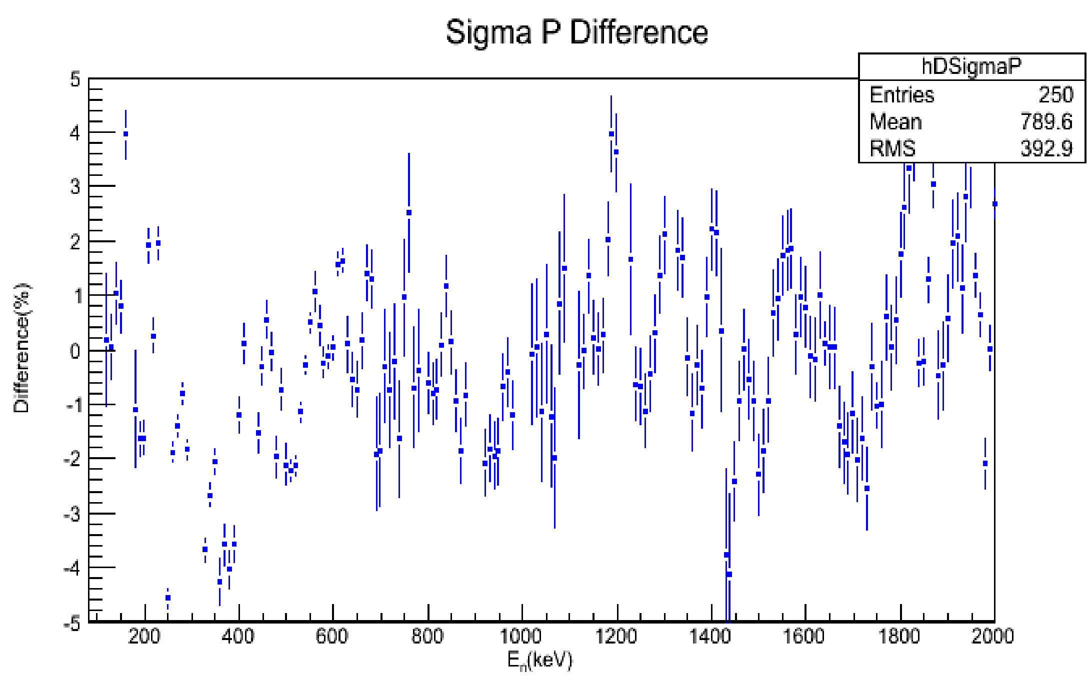

Figure 4.38: The final n-p cross sections (σ_p) in comparison to ENDF tabulated data in the higher-energy region; data are from the Sept. 2014 run.

4.7 Fitting of Effective Range Theory

To fit the result by effective range theory, ENDF (Evaluated Nuclear Data File) obtained from NNDC (National Nuclear Data Center) was used at higher energies above 500 keV along with the our results below 500 keV. Using the equations for effective range theory as described in Section 1.2, we can do the fitting. The parameters from the fit and the previous fit done by Hackenburg [43] are shown in Table 4.1. In general, The results of our fit are in good agreement with the results obtained by Hackenburg. The first set of result is derived by cross section data with no simulation correction. The second set is done after applied simulation correction. As we can see after the correction is applied, the results are getting close to Hackenburg's result.

Since this correction is only preliminary, further consideration is excepted to come later. Our fit is shown with the data in Figure 4.39 and Figure 4.40.

Table 4.1: Parameters from effective range theory fit to our present results, compared to fit by Hackenburg [43]

Parameter	This Work	With Monte Carlo correction	Hackenburg
σ_0	20.4278 b		20.4278 b
	(0.0078)		(0.0078)
a_c	-3.7406 fm		-3.7406 fm
	(0.0010)		0.0010
r_{s0}	0.8746 fm	2.2603 fm	2.75 - 0.059_{syst} fm
	(0.189)	(0.211)	(0.018_{stat})
a_t	5.1655 fm	5.3193 fm	5.4112 fm
	(0.0027)	(0.0280)	(0.0015)
a_s	-23.3002 fm	-24.0117 fm	-23.7148 fm
	(0.0612)	(0.0468)	(0.0043)
$\rho_t(0, -\epsilon_t)$	1.6657 fm	1.7580 fm	1.7436 fm
	(0.0162)	(0.0168)	(0.0019)
χ^2_ν	4.131	2.823	0.749
ν	230	230	817

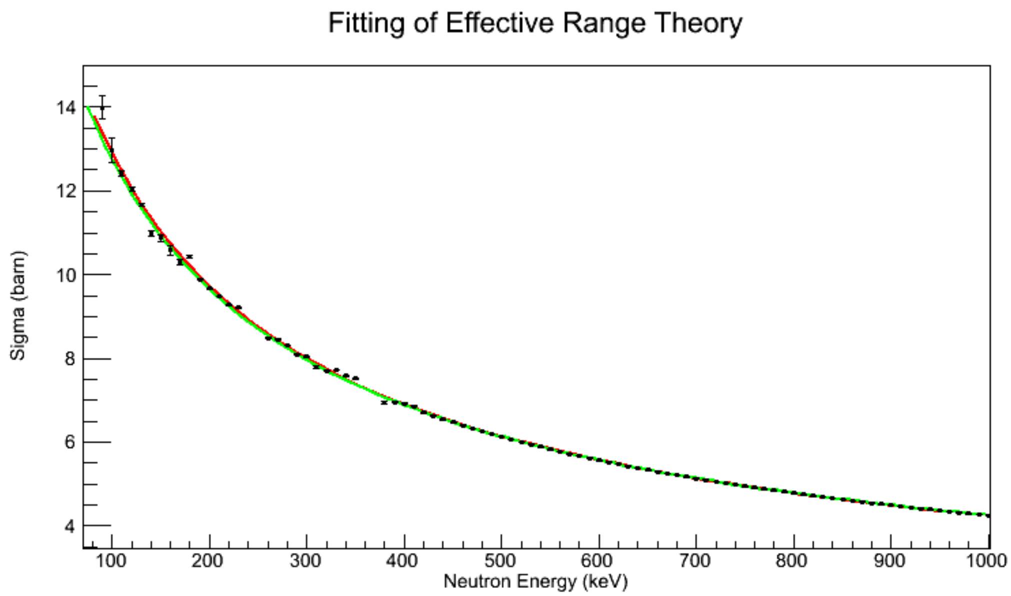

Figure 4.39: Fitted result through effective range theory plotted along with experimental results. Red line is fitted line; green line is plotted using parameters obtained by Hackenburg [43].

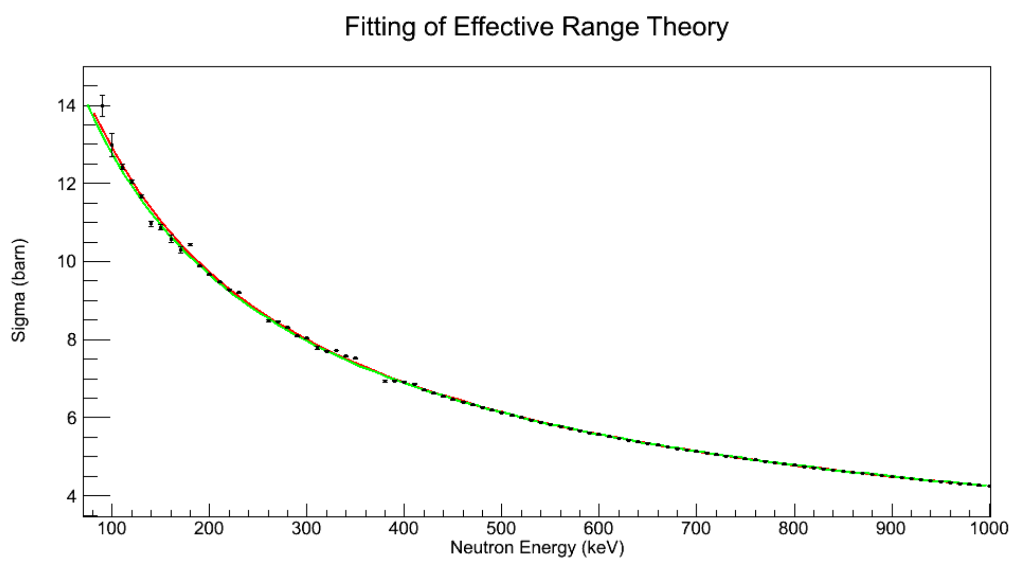

Figure 4.40: Fitted result through effective range theory plotted along with experimental results, simulation correction applied. Red line is fitted line; green line is plotted using parameters obtained by Hackenburg [43].

Chapter 5 Future Work

5.1 n-B cross section

The $^{10}B(n, D)$ and $^{10}B(n, \alpha_1\gamma)$ standards have received considerable attention as a result of the relatively poor database and the problems they caused in the ENDF/B-VI standards evaluation process [46]. They can be measured using the same technique as introduced in this work.

Appendix A Run Directory

Table A.1: Aug. 2014 Run

Run#	Date	E_p (MeV)	E_n (MeV)	Trig(s^{-1})	Atten	Comment
105	08/21	—	—	—	1	^{241}Am
113	08/21	2.41	0.690	1900	1	1874.96kHz
114	08/21	2.41	0.690	1800	1	1874.96kHz
115	08/21	2.50	0.780	1600	1	1874.96kHz
118	08/21	2.50	0.780	1800	1	1874.96kHz
119	08/21	2.60	0.890	1800	1	1874.96kHz
121	08/21	2.60	0.890	1700	1	1874.96kHz
125	08/22	—	—	—	1	^{241}Am
126	08/22	2.70	0.996	1000	1	1874.96kHz
127	08/22	2.70	0.996	1100	1	1874.96kHz
128	08/22	2.80	1.099	1000	1	1874.96kHz
130	08/22	2.90	1.2	1000	0.8	1874.96kHz
133	08/22	2.90	1.2	1000	0.8	1874.96kHz
134	08/22	—	—	—	0.8	^{241}Am
135	08/22	—	—	—	0.7	^{241}Am
136	08/22	—	—	—	0.7	12h BG run
138	08/23	3.0	1.3	1100	0.7	1874.96kHz
139	08/23	3.0	1.3	1200	0.7	1874.96kHz
141	08/23	3.1	1.4	700	0.6	1874.96kHz
143	08/23	—	—	—	0.6	^{241}Am
151	08/28	3.1	1.4	1200	0.6	1874.96kHz
153	08/29	—	—	—	0.5	^{241}Am
154	08/29	3.2	1.5	1600	0.5	1874.96kHz
157	08/29	3.2	1.5	1250	0.5	1874.96kHz
159	08/29	3.3	1.6	1600	0.5	1874.96kHz
160	08/29	3.3	1.6	1700	0.5	1874.96kHz
161	08/30	3.4	1.7	2200	0.5	1874.96kHz
162	08/30	3.4	1.7	2200	0.5	1874.96kHz
163	08/30	3.5	1.8	1800	0.5	1874.96kHz
164	08/30	3.5	1.8	1800	0.5	1874.96kHz
165	08/30	3.6	1.9	1500	0.5	1874.96kHz
166	08/30	3.6	1.9	1500	0.5	1874.96kHz

Table A.2: Sept. 2014 Run

Run#	Date	E_p (MeV)	E_n (MeV)	Trig(s^{-1})	Atten	Comment
301	09/25	3.70	2.02	1150	0.4	1874.96kHz
302	09/25	3.70	2.02	1150	0.4	2 hour run
304	09/25	3.74	2.06	800	0.4	1874.96kHz
305	09/25	3.74	2.06	700	0.4	1874.96kHz
306	09/25	3.74	2.06	800	0.4	1874.96kHz
307	09/26	—	—	—	0.4	^{241}Am
308	09/26	—	—	—	0.4	^{137}Cs
309	09/26	—	—	—	0.3	^{1237}Cs
310	09/26	3.78	2.10	850	0.3	1874.96kHz
311	09/26	3.78	2.10	850	0.3	1874.96kHz
312	09/26	3.78	2.10	850	0.3	1874.96kHz
313	09/26	3.78	2.10	660	0.3	1874.96kHz
314	09/26	3.82	2.14	600	0.3	1874.96kHz
315	09/26	3.82	2.14	600	0.3	1874.96kHz
316	09/26	3.82	2.14	600	0.3	1874.96kHz
317	09/26	—	—	—	0.3	Pedstal
318	09/28	2.35	0.63	1100	1	1874.96kHz
319	09/28	2.35	0.63	1100	1	1874.96kHz
320	09/28	2.35	0.63	800	1	1874.96kHz
321	09/28	2.28	0.55	750	1	1874.96kHz
322	09/28	2.28	0.55	750	1	1874.96kHz
323	09/28	2.28	0.55	750	1	1874.96kHz
324	09/28	—	—	—	0.4	^{241}Am
328	09/29	2.21	0.47	480	1	1874.96kHz
329	09/29	2.21	0.47	480	1	1874.96kHz
330	09/29	2.21	0.47	480	1	1874.96kHz
331	09/29	2.15	0.41	280	1	1874.96kHz
332	09/29	2.15	0.41	280	1	1874.96kHz
333	09/29	2.15	0.41	280	1	1874.96kHz
334	09/29	2.15	0.41	280	1	1874.96kHz
335	09/30	—	—	—	1	^{241}Am
336	09/29	2.10	0.35	280	1	1874.9xkHz
337	09/29	2.10	0.35	300	1	1874.9xkHz
338	09/29	2.10	0.35	300	1	1874.9xkHz
339	09/29	2.10	0.35	300	1	1874.9xkHz
340	09/29	2.10	0.35	300	1	1874.9xkHz
341	09/29	2.10	0.35	300	1	1874.9xkHz
342	09/29	2.10	0.35	280	1	1874.96kHz
343	09/30	—	—	—	1	^{241}Am
344	10/01	2.05	0.29	400	1	1874.96kHz
345	10/01	2.05	0.29	400	1	1874.96kHz

Continued on next page

Table A.2 – Continued from previous page

Run#	Date	E_p (MeV)	E_n (MeV)	Trig(s^{-1})	Atten	Comment
346	10/01	2.05	0.29	400	1	1874.96kHz
347	10/01	2.05	0.29	350	1	1874.96kHz
348	10/01	2.05	0.29	350	1	1874.96kHz
349	10/01	2.05	0.29	330	1	1874.96kHz
350	10/01	—	—	—	1	^{241}Am
352	10/02	2.05	0.29	230	1	937.48kHz
353	10/02	2.05	0.29	230	1	937.48kHz
354	10/02	2.05	0.29	230	1	937.48kHz
356	10/02	—	—	—	1	^{241}Am
359	10/03	2.00	0.23	250	1	937.48kHz
360	10/03	2.00	0.23	250	1	937.48kHz
362	10/03	2.00	0.23	250	1	937.48kHz
363	10/03	2.00	0.23	270	1	937.48kHz
366	10/03	2.00	0.23	240	1	937.48kHz
367	10/03	2.00	0.23	240	1	937.48kHz
368	10/03	1.95	0.17	200	1	937.48kHz
369	10/03	1.95	0.17	200	1	937.48kHz
370	10/03	1.95	0.17	200	1	937.48kHz
371	10/03	1.95	0.17	200	1	937.48kHz
372	10/03	1.95	0.17	200	1	937.48kHz
373	10/03	1.95	0.17	200	1	937.48kHz
374	10/04	—	—	—	1	1am ^{241}Am

Table A.3: Feb. 2015 Run

Run#	Date	E_p (MeV)	E_n (MeV)	Trig(s^{-1})	Atten	Comment
006	02/03	2.15	0.40	900	1	1874.9xkHz
007	02/03	2.15	0.40	900	1	1874.9xkHz
008	02/03	2.15	0.40	900	1	1874.9xkHz
009	02/03	2.15	0.40	800	1	1874.9xkHz
010	02/03	—	—	—	1	^{241}Am
011	02/03	—	—	—	1	100ns delay Calib
012	02/04	2.10	0.35	750	1	1874.9xkHz
013	02/04	2.10	0.35	800	1	1874.9xkHz
014	02/04	2.10	0.35	750	1	1874.9xkHz
015	02/04	2.10	0.35	770	1	1874.9xkHz
016	02/04	2.10	0.35	770	1	1874.9xkHz
017	02/04	2.10	0.35	750	1	2h run
018	02/04	2.10	0.35	700	1	1874.9xkHz
019	02/05	2.06	0.30	850	1	1874.9xkHz
020	02/05	2.06	0.30	850	1	1874.9xkHz
026	02/05	2.06	0.30	820	1	1874.9xkHz
027	02/05	2.06	0.30	800	1	1874.9xkHz
028	02/05	2.06	0.30	800	1	1874.9xkHz
029	02/05	2.06	0.30	750	1	1874.9xkHz
030	02/05	2.06	0.30	750	1	1874.9xkHz
031	02/05	2.06	0.30	750	1	1874.9xkHz
033	02/06	2.00	0.23	730	1	1874.9xkHz
034	02/06	2.00	0.23	700	1	2h run
035	02/06	2.00	0.23	650	1	1874.9xkHz
036	02/06	2.00	0.23	600	1	1874.9xkHz
037	02/06	2.00	0.23	600	1	1874.9xkHz
038	02/06	2.00	0.23	580	1	1874.9xkHz
039	02/06	2.00	0.23	560	1	1874.9xkHz
040	02/07	1.96	0.18	680	1	new LiF
041	02/07	1.96	0.18	650	1	1874.9xkHz
042	02/07	1.94	0.15	620	1	1874.9xkHz
043	02/07	1.94	0.15	630	1	1874.9xkHz
044	02/07	1.94	0.15	750	1	1874.9xkHz
045	02/07	1.92	0.13	750	1	1874.9xkHz
046	02/07	1.92	0.13	750	1	1874.9xkHz
047	02/07	1.92	0.13	770	1	1874.9xkHz
048	02/07	—	—	—	1	^{241}Am
050	02/08	—	—	—	1	Calibrator Calib

Bibliography

[1] R Machleidt and I Slaus, *The nucleon-nucleon interaction*, 2001 J. Phys. G: Nucl. Part. Phys. 27 R69

[2] Yukawa H, 1935. Proc. Phys. Math. Soc. Japan 17 48.

[3] Slaus I, Akaishi Y and Tanaka H 1989 Phys. Rep. 173 257.

[4] Miller G A, Nefkens M K, and Slaus I 1990 Phys. Rep. 194 1.

[5] Miller G A and van Oers W H T 1995, *Symmetries and Fundamental Interactions in Nuclei*, Haxton W C and Henley E M (ed) (Singapore: World Scientific) p 127

[6] Machleidt R, Holinde K, and Elster C 1987 Phys. Rep. 149 1

[7] Li G Q and Machleidt R 1998 Phys. Rev. C 58 3153

[8] Particle Data Group 2000 Eur. Phys. J. C 15 1

[9] Ericson T E O and Miller G A 1983 Phys. Lett. 132B 32

[10] Banerjee M K 1975, *Electromagnetic Interactions of Nucleons*, University of Maryland Technical Report No. 75-05

[11] Chemtob M 1975, *Interaction Studies in Nuclei*, edited by Jochim H and Ziegler B (Amsterdam:North-Holland) p 487

[12] van Kolck U, Rentmeester M C M, Friar J L, Goldman T, and de Swart J J 1998 Phys. Rev. Lett. 80 4386

[13] H. A. Bethe and R. E. Peierls, Proc. Roy. Soc. A148, 146 (1935).

[14] E. Fermi and L. Marshall, *Interference Phenomena of Slow Neutrons*, Phys. Rev. 71, 666 Published 15 May 1947.

[15] F. C. Barker and R. E. Peierls, Phys. Rev. 75, 312 (1949), have given a similar derivation for the effective range. Also similar are the calculations of G. F. Chew and M. L. Gold-berger, Phys. Rev. 75, 1637 (1949).

[16] J. M. Blatt and J. D. Jackson, Phys. Rev.

[17] J. Schwinger, *Harvard lecture notes*(hectographed only).

[18] R. Wilson, *The Nucleon-Nucleon Interaction, Experimental and Phenomenological Aspects*, (Interscience, New York, 1963).

[19] H. A. Bethe, Phys. Rev. 76, 38 (1949).

[20] Y. Fujita, K. Kobayashi, T. Oosaki, and R. C. Block, Nucl. Phys. A258, 1 (1976).

[21] E. E. Lampi, G. D. Freier, and J. H. Williams, Phys. Rev. 80, 853 (1950); data from CINDA, file EXFOR 12644.003.

[22] A.O. Hanson and J.L. McKibben. 1947. Phys. Rev. 72: 673.

[23] W.D. Allen. 1960, *Flat Response Counters in Fast Neutron Physics Part 1*, J.B. Marion and J.L. Fowler, editors. Interscience, (NY), 361.

[24] Glenn F. Knoll. 2000, *Radiation Detection and Measurement (3rd ed.)*, John Wiley & Sons, 542.

[25] K. Shibata, *JENDL 3.3 Evaluation, material 125*, 2002.

[26] G. M. Hale and A. S. Johnson in Proc. 17th Int. IUPAP Conf. on Few-Body Problems in Physics, 5-10 June 2003 (W. Gloeckle and W. Tornow, eds.), (Durham NC), pp. S120S122, Elsevier B.V., 2004.

[27] D. H. Frisch, *The Total Cross Sections of Carbon and Hydrogen for Neutrons of Energies from 35 to 490 kev*, Phys. Rev., vol. 70, pp. 589592, Nov 1946.

[28] A. L. Kirilyuk, A. V. Grebnev, P. N. Vorona, and N. L. Gnidak C87KIEV2, vol. 289, 1987.

[29] C. E. Engelke, R. E. Benenson, E. Melkonian, and J. M. Lebowitz, *Precision Measurements of the n p Total Cross Section at 0.4926 and 3.205 MeV*, Phys. Rev., vol. 129, pp. 324337, Jan 1963.

[30] L. Koester, W. Waschkowski, and J. Meier, *Cross sections for neutrons of 1970 ev and contributions to fundamental neutron interactions*, Zeitschrift fr Physik A Hadrons and Nuclei, vol. 337, pp. 341348, 1990. 10.1007/BF01289703.

[31] W. D. Allen and A. T. G. Ferguson, emphThe n-p Cross Section in the Range 60-550 keV, Proceedings of the Physical Society. Section A, vol. 68, no. 11, p. 1077, 1955.

[32] C. L. Bailey, W. E. Bennett, T. Bergstralth, R. G. Nuckolls, H. T. Richards, and J. H. Williams, *The neutron-proton and neutron-carbon scattering cross sections for fast neutrons*, Phys. Rev., vol. 70, pp. 583589, Nov 1946.

[33] J. Clement, P. Stoler, C. Goulding, and R. Fairchild, *Hydrogen and deuterium total neutron cross sections in the MeV region*, Nuclear Physics A, vol. 183, no. 1, pp. 51 59, 1972.

[34] W. P. Poenitz and J. F. Whalen, *Measurements of the total neutron cross sections of hydrogen and carbon at 0.5, 1.0 and 2.0 MeV*, Nuclear Physics A, vol. 383, no. 2, pp. 224 232, 1982.

[35] E. Bretscher and E. B. Martin, *Determination of the collision cross section of hydrogen, deuterium, carbon, and oxygen for fast neutrons*, Helvetica Physica Acta, vol. 23, p. 15, 1950.

[36] D. S. S. et. al., *Precision neutron transmission and energy measurement by time-of-flight*, 3rd Conf. Neutron Cross-Sections and Tech., vol. 2, p. 543, 1971.

[37] H. Liskien and A. Paulsen, *Neutron production cross sections and energies for the reactions 7 Li(p,n)7 Be and 7 Li(p,n)7 Be*, Atomic Data and Nuclear Data Tables, vol. 15, no. 1, pp. 57 84, 1975.

[38] H. Liskien and A. Paulsen, *Neutron production cross sections and energies for the reactions T(p,n)3 He, D(d,n)3 He, and T(d,n)4 He*, Atomic Data and Nuclear Data Tables, vol. 11, no. 7, pp. 569 619, 1973.

[39] C.A. Goulding et al, *Comparison of the Scintillators BC-501 and NE213*, LANL Technical Note LA-N2TN-87-201, April 1987.

[40] F.T. Kuchnir & F.J. Lynch, *Time-Dependence of Scintillators and the Effect on P.S.D.*, IEEE Trans. Nucl. Sci., NS-15, No. 3, 107-113 (1968)

[41] J.B.Czirr, *The Alpha/Beta Ratio of Several Organic Scintillators*, Nucl. Instr. & Meth., 161, 439-447 (1979).

[42] R. Katz et al, Nucl Instr. & Meth., 100, 13-32 (1972).

[43] R. W. Hackenburg, *Neutron-proton effective range parameters and zero energy shape dependence*, Phys. Rev. C, vol. 73, p. 044002, Apr 2006.

[44] B. H. Daub,1, V. Henzl,1, M. A. Kovash,2 J. L. Matthews,1 Z. W. Miller,2 K. Shoniyozov,2 and H. Yang, *Measurements of the neutron-proton and neutron-carbon total cross section from 150 to 800 keV*, Phys. Rev. C 87, 014005 (2013).

[45] Brian Daub, *Low Energy Neutron-Proton Interactions*, Massachusetts Institute of Technology, 2012.

[46] *International Evaluation of neutron Cross-Section Standards*, International Atomic Energy Agency, 2007.

Vita

Hongwei Yang

2001-2005 B.S. degree of Applied physics in Southeast University
2006-2009 M.S. degree of Theoretical physics in Southeast University
2009-2011 M.S. degree of Physics & Astronomy in University of Kentucky
2011-2015 Ph. D. student in University of Kentucky

Professional publications:

[1] B. H. Daub, V. Henzl, M. A. Kovash, J. L. Matthews, Z. W. Miller, K. Shoniyozov, and H. Yang, *Measurements of the neutron-proton and neutron-carbon total cross section from 150 to 800 keV*, Physical Review C 87, 014005 (2013) .

[2] B.H. Daub, V. Henzl, M.A. Kovash, J.L. Matthews, Z.W. Miller, K. Shoniyozov, H. Yang, *Response of BC-418 plastic scintillator to low-energy protons*, Nuclear Instruments and Methods in Physics Research A 701 (2013) 171175 .

[3] W. Ye, F. Wu, H.W. Yang, *A note on the examination of isospin effects in multi-dimensional Langevin fission dynamics*, Physics Letters B 700 (2011) 362364.

[4] W. Ye, H. W. Yang, and F. Wu, *Isospin effects on the evaporation residue spin distribution*, Physical Review C 77, 011302(R) (2008) .

[5] W. Ye, F. Wu, H.W. Yang, *Isospin effect on pre-scission γ emission*, Physics Letters B 647 (2007) 118121.

[6] YE Wei, YANG Hong-Wei, *Effects of N/Z on survival probability of heavy nuclei*, Chinese Physics C (HEP & NP) . Vol. 32, No. 1, Jan., 2008 .

[7] YANG Hong-Wei, YE Wei, *Spin distribution of evaporation residue cross section within a stochastic approach*, Chinese Physics C (HEP & NP) . Vol. 32, No. 3, Mar., 2008 .

[8] YE Wei, WU Feng, YANG Hong-Wei, *Langevin study of neutron emission in the reactions 16 O+181Ta and 19F+178 Hf*, Chinese Physics C (HEP & NP) . Vol. 32, No. 10, Oct., 2008 .

[9] WEI YE, HONG-WEI YANG and FENG WU, *Langevin description of the evaporation residue spin distribution*, International Journal of Modern Physics E . Vol. 17, No. 9 (2008) 18751882 .